On the performance of liquid-liquid Taylor flow electrochemistry in a microreactor – A CFD study

Cao, Y.; Padoin, N.; Soares, C.; Noël, T.

On the performance of liquid-liquid Taylor flow electrochemistry in a microreactor – A CFD study

Yiran Cao [a], Natan Padoin [b,*], Cíntia Soares [b], Timothy Noël [c,*]

[a] Department of Chemical Engineering and Chemistry, Sustainable Process Engineering, Micro Flow Chemistry & Synthetic Methodology, Eindhoven University of Technology, De Rondom 70 (Helix, STO 1.37), 5612 AP Eindhoven, the Netherlands
[b] Department of Chemical and Food Engineering, Federal University of Santa Catarina, Florianópolis, SC 88040-900, Brazil
[c] Van't Hoff Institute for Molecular Sciences (HIMS), University of Amsterdam (UvA), Science Park 904, 1098 XH Amsterdam, the Netherlands

ARTICLE INFO

ABSTRACT

A comprehensive understanding of the underlying phenomena (coupled fluid flow, charge transfer, mass transfer and chemical reaction) is fundamental for a proper design, analysis and scale-out of chemical reactors when carrying out multiphase electro-organic transformations. In this study, we have explored the novel combination of organic electrochemical synthesis and computational fluid dynamics (CFD) to perform a systematic theoretical investigation concerning the effect of different operational parameters on the performance of organic-aqueous Taylor flow in electrochemical microreactors. The results indicate that operating at high concentrations of the rate-limiting species (>5 mol·m^{-3} for $D_i \geq 10^{-9}$ m^2·s^{-1}; 500 mol·m^{-3} for $D_i \sim 10^{-10}$ m^2·s^{-1}) is beneficial for the reactor performance. However, excessively high concentrations (>500 mol·m^{-3}) do not result in a further improvement in mass transfer and current/voltage relation. Higher diffusivities are also beneficial, but even in this scenario limiting current densities can be found when working at low concentrations. Overall, keeping an internal:external phase electrical conductivity ratio > 1 improves the reactor performance. Working at lower velocities can be beneficial in some scenarios, since higher limiting current densities can be obtained. However, the velocity impact on the reactor performance is not significant in some operating conditions (e.g., at higher concentrations and diffusivities). Finally, working with higher cell potentials is beneficial, but limiting current densities can be encountered at lower concentrations and diffusivities. Variables such as internal phase volume fraction, droplet length and interelectrode distance also have relevant impact on the reactor performance, but are subjected to the same conditioning factors previously mentioned. A comprehensive potential balance was also conducted, showing the relative importance of the activation, Ohmic and concentration overpotentials under different operating conditions. We believe the insights gained herein will be of interest to researchers in both academia and industry to develop more efficient electrochemical flow reactors for liquid–liquid transformations.

1. Introduction

There is no doubt about the urgent need for an in-depth assessment of the current industrial standards for chemical transformations to enable greener and more efficient synthetic routes. Smart chemical plants will be required, which use automation and artificial intelligence to adjust the processes in real time, thus establishing highly selective and productive transformations [1,2]. In addition, the sustainability goals of the chemical industry can -at least partially- be achieved through the maxims of process intensification (PI) [3-9].

Multifunctional reactors [10-12], including monolithic designs [13-15], and micro-flow [16,17] devices are the current standards for intensifying chemical transformation plants at the equipment level. Monolithic structures have been applied in electrochemical [18-20], photochemical [21] and thermally-activated catalytic reactions [22,23]. Environmental protection, power plants and bulk chemicals can be listed among several sectors in which this technology has already been implemented, carrying out monophasic or multiphase flows [23]. Similarly, micro-flow chemistry, driven by photochemical [24,25] or electrochemical [26] activation modes, has attracted a great deal of attention in recent years due to the potential to use renewable energy sources. Microreactors have widely been recognized as a key equipment for Process Intensification as they provide high surface-to-volume ratios, short diffusion distances, high and reproducible interfacial areas [27].

Therefore, the combination of microreactors with photo-/electrochemistry is a perfect match to enable green process development focused on high efficiency with a reduction of the negative side effects to our planet.

The increased availability of green electricity has driven smart technologies in several areas, including transportation and the energy sector [28,29]. This fact has also pushed academia and industry towards a renewed interest in developing micro-flow electrochemical methodologies [30]. Electron-driven chemical activation is attractive not only from a sustainability perspective but also as a strategy to establish new synthetic transformations and to provide higher selectivities in conventional synthetic pathways [31,32]. While most of the electroorganic transformations are conducted in single-phase flow (i.e., with all species in solution), multiphase applications involving gas–liquid [33,34] and liquid–liquid flow [35-37], often leading to the so-called Taylor flow [38-40], are also encountered. The segmented flow regime occurring in these devices leads to toroidal fluid circulation patterns [39,40], allowing for increased radial heat and mass transfer while minimizing axial dispersion effects.

The theoretical understanding of the transport phenomena and the charge transfer processes occurring in multiphase micro-flow electrochemistry is of paramount importance for proper design, analysis and scale-out purposes. In a previous study [41] we have used computational fluid dynamics (CFD), a powerful tool for simulating the coupled nonlinear phenomena taking place in micro-flow chemistry [42-48], to investigate the effect of mixing and charge transfer in gas–liquid micro-flow electro-organic transformations. Our calculations have shown that gas bubbles have controversial effects on the performance of these devices. This means that, while the presence of the bubbles intensify the mixing efficiency [49-53], the gas bubbles also block the charge transfer and, thus, the chemical reaction shuts down around them.

Despite the fact that the fluid dynamics [54-57] and the associated heat [58-62] and mass [63-65] transport mechanisms of liquid–liquid flow processes are quite established, theoretical and/or experimental investigations of liquid–liquid electrochemical systems are hitherto only rarely reported [66-69].

To the best of our knowledge, a systematic theoretical investigation of Taylor flow with coupled mass transfer, charge transfer and chemical reaction in liquid–liquid electro-organic transformations is currently missing. More specifically, we were interested in the charge and mass transfer behavior in such liquid–liquid micro-flow systems and the influence of different electrical conductivity ratios. Could the presence of an aqueous phase have a positive effect on electro-organic transformations in comparison to an equivalent homogeneous (single-phase) system? How different would the coupled nonlinear phenomena behave in liquid–liquid electro-organic systems when compared to the gas–liquid ones?

These questions have stimulated us to perform a study focused on the novel combination of CFD and liquid–liquid electro-organic transformations. The effect of different operational variables (electrical conductivity ratio, mass diffusivity, velocity, concentration, cell potential, internal phase volume fraction, internal phase length and interelectrode distance) were systematically studied using CFD calculations. The investigation was mainly based on the analysis of a potential distribution in the electrochemical microreactor (considering the contribution of ohmic, concentration and activation overpotential) and polarization curves. The electrochemical oxidative coupling between thiophenol and fluoride yielding sulfonyl fluorides [70,71]) was selected as a benchmark reaction and a typical modular electrochemical microreactor configuration was considered [72]. We believe that the insights provided herein will aid in the future design, analysis and scale-out of electrochemical flow reactors and the execution of micro-flow electro-organic transformations.

2. Method

2.1. Electrochemical reactor and benchmark reaction

The micro-flow electrochemical reactor (Fig. 1A) designed by our group and described in detail elsewhere [72] was considered for modeling purposes. In summary, the reactor comprises eight channels (allowing for different reactor configurations in series and parallel and consequent variable reaction volume) with an interelectrode distance of 250 μm and a width of 3 mm (Fig. 1B) [71-73]. This device represents a typical electrochemical microreactor for organic transformations, serving as a reference for the interelectrode distances and velocities adopted in our numerical investigations.

Moreover, as a benchmark reaction with the kinetics at the anode as the rate-limiting step, the electrochemical oxidative coupling of thiophenol and fluoride yielding sulfonyl fluoride was considered (Fig. 1C) [71]. The reaction medium consists of a biphasic mixture composed of aqueous HCl solution and an organic CH_3CN phase. Thiophenol is used as the substrate, while KF was the fluoride source. Moreover, pyridine is added to produce high yields since it may act as a phase transfer catalyst and electron mediator, according to the mechanism illustrated in Fig. 1D.

Following the mechanism proposed, reaction (ii) represents the rate-limiting step at the anode [70,74,75], while the other steps are considered to be fast as we were never able to isolate or observe those intermediates under the given reaction conditions. Furthermore, step (i) represents KF association with pyridine and fluoride interfacial transfer from the aqueous to the organic phase. The fluoride phase transfer occurs in the form of $C_5H_5NH^+\cdot F^-$ and controls the supply of this reagent to the anode surface. The optimal reaction condition is achieved with a residence time of 5–10 min and a cell potential of 3.30 V [71]. Again, this reaction environment was taken as a reference for the parametric study carried out numerically herein, considering the effects of different scenarios on the performance of liquid–liquid electrochemical transformations in micro-flow.

2.2. Mathematical modeling and computational procedure

2.2.1. Computational domain

The liquid–liquid flow inside the electrochemical microreactor can be represented by the scheme shown in Fig. 2A, where Ω_1 is the internal (dispersed) phase and Ω_2 is the external (continuous) phase.

Taylor recirculation occurs in the external and internal phases. The subdomain Ω_1 repeats periodically along the reactor. Moreover, each subdomain Ω_1 represents a source for the rate-limiting species *i*. The two-phase flow occurs in the interelectrode gap (cathode placed at the upper plate and anode placed at the bottom plate). The electrochemically-driven chemical transformation occurs only at the anode surface.

The full domain was reduced to a 2D unit cell (UC) for modeling purposes, representing the periodical Taylor flow occurring throughout the reactor, depicted in Fig. 2B. This unit cell was modeled, taking the disperse phase as the reference frame. Therefore, the droplet velocity U_D was imposed at the walls, while a relative velocity ($U_D - U_{TP}$; U_{TP} corresponding to the average two-phase velocity) and null gauge pressure were prescribed at the inlet and the outlet, respectively.

2.2.2. Fluid flow

The multiphase flow in the electrochemical device was calculated through the moving mesh Arbitrary Lagrangian–Eulerian (ALE) formulation [76-79] in COMSOL® Multiphysics. This enables precise flux calculations at fluid–fluid interfaces. Moreover, it allows a straightforward implementation of fluxes at fluid–fluid interfaces. Working with the moving mesh approach also provides an easy implementation of a known saturation concentration or a partition coefficient at the interface. Additionally, growth or shrinkage of the dispersed phase due to
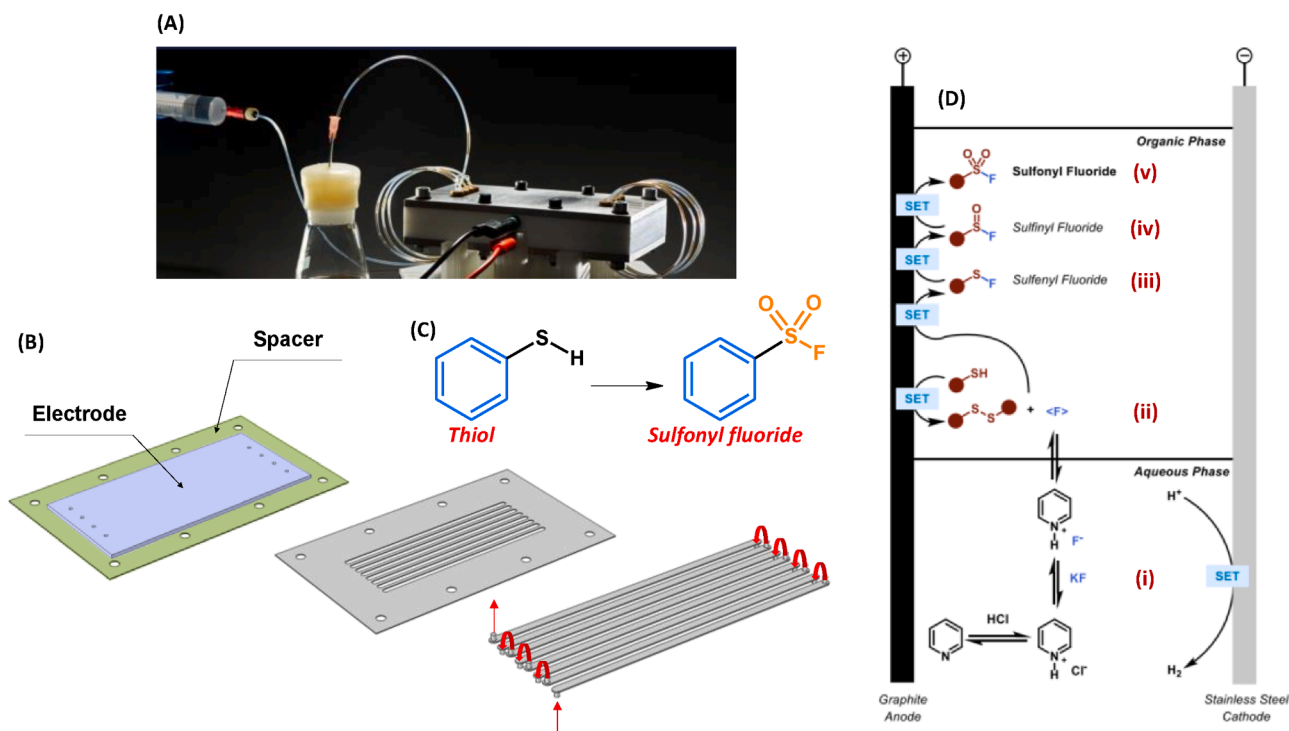
Fig. 1. Overview of the reaction environment: (A) electrochemical reactor – external view, (B) electrochemical reactor – internal view, (C) chemical transformation under study, and (D) reaction mechanism (reaction *ii* represents the rate limiting step at the anode's surface, since the steps *iii-v* represent click reaction mechanisms; step *i* represents KF dissociation, mediated by pyridine, and fluoride interfacial transfer from the aqueous to the organic phase).
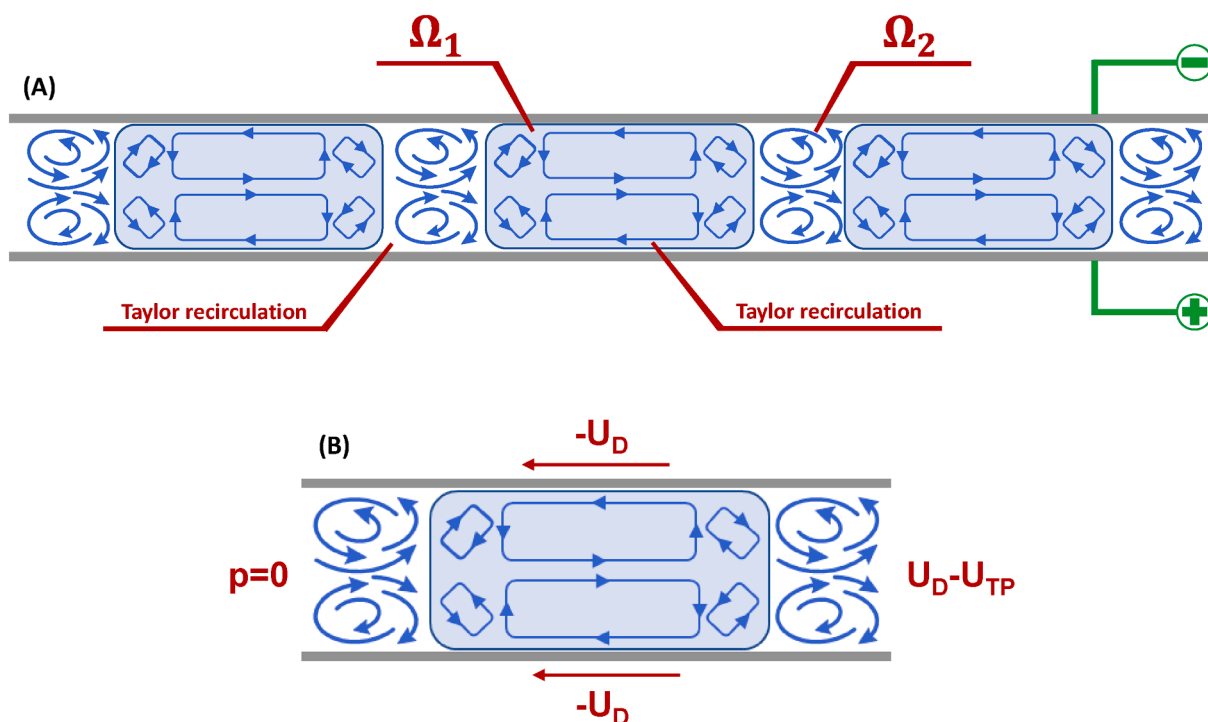

Fig. 2. Biphasic flow occurring in the electrochemical reactor: (A) segmented flow (internal phase Ω_1 and external phase Ω_2 flowing periodically between the electrodes), and (B) a scheme of the unit cell considered in this work, with an indication of the boundary conditions adopted.

mass transfer at the interface can be easily implemented in COMSOL® Multiphysics using the moving mesh approach. Given the advantages of this method for the current and future investigations in this field, we have opted to use this approach in our simulations as an alternative to traditional multiphase models (e.g., level-set, phase field, etc.).

The two-dimensional, Newtonian, transient, laminar and incompressible flow occurring in the micro-electrochemical device was modeled according to Eqs. (1) and (2) (momentum and overall mass conservation, respectively):

$$\rho\left[\frac{\partial u}{\partial t} + (u_c \bullet \nabla)u\right] = \nabla \bullet \left[-pI + \mu\left(\nabla u + (\nabla u)^T\right)\right] \tag{1}$$

$$\nabla \bullet u = 0 \tag{2}$$

where u_c (m·s^{-1}) is the convective velocity, defined as the difference of material velocity and mesh velocity [76], and u (m·s^{-1}) is the velocity. The gravitational force was neglected (since viscous forces and surface tension are predominant, $B_o = \Delta\rho gD^2/\sigma = 0.13$)

At the inlet, fully developed laminar flow was adopted, while at the outlet, null gauge pressure was specified. At the upper and bottom walls, a tangential velocity was specified according to Eq. (3).

$$u = U_w t \tag{3}$$

where U_w (m·s^{-1}) is the velocity imposed at these boundaries and t (dimensionless) is the tangential vector at the walls.

At the liquid–liquid interface, the finite stresses are calculated according to Eq. (4) [76].

$$n \bullet \tau_1 = n \bullet \tau_2 + f_{st} \tag{4}$$

where τ_1 (N·m^{-2}) and τ_2 (N·m^{-2}) are the total stress tensors in each phase (internal and external, respectively) at the interface, while n (dimensionless) is the normal of the interface. The term f_{st} (N·m^{-2}) corresponds to the force per unit area related to the surface tension, expressed in Eq. (5) [76].

$$f_{st} = \sigma(\nabla_s \bullet n)n - \nabla_s\sigma \tag{5}$$

where σ is the surface tension coefficient (N·m^{-1}) and ∇_s is the surface gradient operator, given by Eq. (6) [76].

$$\nabla_s = (I - n \bullet n^T)\nabla \tag{6}$$

Two components (normal and tangential) can be written for the surface tension, according to Eqs. (7) and (8), respectively [76].

$$(n \bullet \tau_1 - n \bullet \tau_2) \bullet n = \sigma\kappa \bullet n \tag{7}$$

$$(n \bullet \tau_1 - n \bullet \tau_2) \bullet t = 0 \tag{8}$$

where κ (dimensionless) is the curvature of the interface. Moreover, continuity of the velocity field is considered at the interface, according to Eq. (9) [76].

$$u_1 = u_2 \tag{9}$$

where u_1 (m·s^{-1}) and u_2 (m·s^{-1}) are the velocity of the internal and external phase, respectively, at the interface.

2.2.3. Mass transfer and chemical reaction

The transport of species i in the micro-electrochemical reactor was modeled through the steady-state convection–diffusion equation (Eq. (10)), neglecting any bulk chemical reaction and considering Fickian diffusive flux.

$$(u_c \bullet \nabla)c_i = \nabla \bullet (D_i\nabla c_i) \tag{10}$$

where u_c (m·s^{-1}) is the convective velocity, c_i (mol·m^{-3}) is the species i molar concentration and D_i (m^2·s^{-1}) is the species i mixture diffusivity (assumed as constant).

A finite flux was taken into account for species i, dependent on the local current density, at the anode's surface (Eq. (11)), while the diffusive flux was assumed as negligible at the cathode's surface (Eq. (12)).

$$-r_i^{''} = \frac{\nu_i i_{loc}}{nF} \tag{11}$$

$$-n \bullet J_i = 0 \tag{12}$$

where $-r_i^{''}$ is the rate of species i consumption per unit of the anode's surface area (mol·m^{-2}·s^{-1}), ν_i is the stoichiometric coefficient (dimensionless), i_{loc} is the position-dependent current density (A·m^{-2}), n is the

number of electrons involved in the chemical transformation (dimensionless), F is the Faraday constant (C·mol^{-1}) and n is the normal vector (dimensionless).

Periodicity was assigned at the unit cell's lateral boundaries, as described by Eqs. (13) and (14), i.e., both the species i concentration and normal convective flux are equal at these frontiers.

$$c_{isrc} = c_{idst} \tag{13}$$

$$-n_{src} \bullet (J_i + uc_i)_{src} = n_{dst} \bullet (J_i + uc_i)_{dst} \tag{14}$$

where c_{isrc} and c_{idst} are the species i concentration (mol·m^{-3}) at the source and destination boundaries, respectively; n_{src} and n_{dst} (dimensionless) are the normal vectors at the source and destination boundaries, respectively. The source and destination boundaries for the species transport model are equivalent to the inlet and outlet boundaries, respectively, of the fluid flow model.

Moreover, the concentration of species i was imposed as the saturation concentration at the fluid–fluid interface, according to Eq. (15).

$$c_i = c_{i,int} = c_{i,sat} \tag{15}$$

where $c_{i,sat}$ is the species i's saturation concentration (mol·m^{-3}).

2.2.4. Electrochemistry

The unit cell's electrochemistry was solved through a steady-state secondary current distribution approach, accounting for the concentration gradient and electrode kinetics. The electrolyte (phases Ω_1 and Ω_2) was assumed to conduct current according to Ohm's law (Eqs. (16) and (17)).

$$i_l = -\sigma_l\nabla\phi_l \tag{16}$$

$$\nabla \bullet i_l = 0 \tag{17}$$

where i_l (A·m^{-2}) is the current density vector, σ_l (S·m^{-1}) is the electrical conductivity and ϕ_l (V) is the electrolyte potential. The conductivity of each phase (σ_{l,Ω_1} and σ_{l,Ω_2}) was constant. However, the values attributed to σ_{l,Ω_1} and σ_{l,Ω_2} were systematically varied in this study.

Null electric flux was assigned to the unit cell's lateral boundaries (Eq. (18)), ensuring periodicity.

$$-n \bullet i_l = 0 \tag{18}$$

where n (dimensionless) is the normal vector.

On the other hand, the electric flux assumed finite values at the electrodes (Eq. (19)), which in a generic case can be expressed as the sum of the local current densities from the m chemical reactions occurring at those boundaries (Eq. (20)).

$$n \bullet i_l = i_{total} \tag{19}$$

$$i_{total} = \sum_m i_{loc,m} = i_{loc} \tag{20}$$

where i_{total} (A·m^{-2}) is the total current density arising from the m chemical reactions occurring at the electrode's surface. In this study, $m = 1$ and i_{total} is equal to the position-dependent current density i_{loc} (A·m^{-2}).

In particular, concentration-dependent kinetics was prescribed at the anode (Eq. (21)) to account for the current density at that surface, while linearized Butler-Volmer kinetics was assumed at the cathode (Eq. (22)).

$$i_{loc} = i_0\left[c_R exp\left(\frac{\alpha_a F\eta}{RT}\right) - c_O exp\left(\frac{\alpha_c F\eta}{RT}\right)\right] \tag{21}$$

$$i_{loc} = i_0\left[\frac{(\alpha_a + \alpha_c)F}{RT}\right]\eta \tag{22}$$

where i_{loc} (A·m^{-2}) is the local current density, F (C·mol^{-1}) is the Faraday constant, i_0 (A·m^2) is the exchange current density, c_R and c_O

(dimensionless) are the concentration of reduced and oxidized species, respectively, α_a and α_c (dimensionless) are the anodic and cathodic transfer coefficients, respectively, R (J·mol^{-1}·K^{-1}) is the universal gas constant, T (K) is the temperature and η (V) is the overpotential.

The overpotential η was calculated according to Eq. (23), where ϕ_s (V) and ϕ_l (V) are the electrode and electrolyte potential, respectively, and E_{eq} (V) is the equilibrium potential. Finally, a comprehensive potential balance was carried in the system, accounting for the activation (η_a and η_c, at the anode and the cathode, respectively), the ohmic (η_{ohm}) and the concentration (η_{conc}) overpotentials, according to Eq. (24).

$$\eta = \phi_s - \phi_l - E_{eq} \tag{23}$$

$$E_{cell} = E_{eq} + \eta_a + \eta_c + \eta_{ohm} + \eta_{conc} \tag{24}$$

2.2.5. Computational procedure

2.2.5.1. Computational domain and solution strategy. We started the simulations by solving the fluid dynamics in the 2D unit cell. A UC with height $H = 250$ μm and length $4H$ was taken as reference. The ratio $\gamma = \Omega_1/\Omega_2$ was initially fixed in 0.5. An arbitrary shape for the secondary phase (Ω_2) was considered. Given the boundary conditions imposed, a time-dependent solution of the fluid flow equations was performed until steady-state was reached. An iterative procedure was adopted to find the wall velocity (U_w) resulting in steady-state conditions, i.e., stable secondary phase morphology with negligible interface motion positioned at the center of the UC, for a given set of boundary conditions. Three velocities were considered though a multiplier $\beta = 1 - 3$ ($\beta = 3$ corresponding to the velocity leading to the residence time of 5 min – typical in liquid–liquid electroorganic transformations in microchannels; $\beta_2 = \beta_3/2$ and $\beta_1 = \beta_3/3$). The surface tension coefficient was defined as 1 mN·m^{-1} in all simulations. Surface tension coefficients for aqueous-organic pairs typically vary in the range of $\sim$ 1 mN/m to $\sim$ 50 mN/m [80]. The external phase consists of CH$_3$CN, with density of 786 kg·m^{-3} and dynamic viscosity of 0.341 mPa·s, while the internal phase is water, with density of 1000 kg·m^{-3} and dynamic viscosity of 1 mPa·s.

2.2.5.2. Validation of the fluid flow model. Based on the same approach, different configurations were tested varying the two-phase velocity in the UC (U_{TP}), the UC length keeping γ constant (elongated secondary phase), the UC length with variable γ and the UC height H.

The same procedure was also applied to verify the fluid flow model, taking the thin film formed between the interface and the walls (external phase, Ω_2, film thickness), the droplet (internal phase, Ω_1) velocity and the pressure drop per droplet (internal phase, Ω_1) as reference. The numerical results for the external phase film thickness was compared with the predictions from the correlations developed or modified by Bretherton [81], Aussillous and Quéré [82], Han, Shikazono and Kasagi [83] and Eain, Egan and Punch [84] according to Eqs. (25)–(28), respectively.

$$\frac{\delta}{D} = \frac{1}{2} \cdot 0.643 \cdot (3 \cdot \text{Ca}_D)^{2/3} \tag{25}$$

$$\frac{\delta}{D} = \frac{1}{2} \cdot \frac{0.643 \cdot (3 \cdot \text{Ca}_D)^{2/3}}{1 + 2.5 \cdot 0.643 \cdot (3 \cdot \text{Ca}_D)^{2/3}} \tag{26}$$

$$\frac{\delta}{H} = \frac{0.670 \cdot Ca_D^{2/3}}{1 + 3.13 \cdot Ca_D^{2/3} + 0.504 \cdot Ca_D^{0.672} \cdot Re_D^{0.589} - 0.352 \cdot We_D^{0.0629}} \tag{27}$$

$$\frac{\delta}{D} = \frac{1}{2} \cdot \frac{0.643 \cdot (3 \cdot \text{Ca})^{2/3}}{1 + 1.6 \cdot 0.643 \cdot (3 \cdot \text{Ca})^{2/3}} \tag{28}$$

where δ (m) is the thin film thickness, D (m) is the channel's diameter, H (m) is the channel's height, Ca_D (dimensionless) is the capillary number based on the dispersed phase velocity ($Ca_D = \mu_{ext} U_D/\sigma$; μ_{ext}

consisting in the dynamic viscosity of the external phase) and Ca is the capillary number based on the average two-phase velocity ($Ca = \mu_{ext} U_{TP}/\sigma$).

The droplet velocity was calculated as a function of the average two-phase velocity, the film thickness (predicted by a correlation) and the channel's characteristic length according to Eq. (29) [85].

$$\frac{U_D}{U_{TP}} = \left(1 - 2 \cdot \frac{\delta}{D}\right)^{-2} \tag{29}$$

Moreover, the pressure drop per droplet was estimated using the correlations of Ratulowski and Chang [86] and Langewisch and Buongiorno [87], according to Eqs. (30) and (31), respectively.

$$\frac{\Delta P_D}{\sigma/R} = 4.52 \cdot (3 \cdot \text{Ca}_D)^{2/3} - 12.6 \cdot \text{Ca}_D^{0.95} \tag{30}$$

$$\frac{\Delta P_D}{\sigma/R} = \begin{cases} 3.96 \cdot Ca_D^{0.58}, Ca_D < 0.187, Re_D < 5 \\ 8 \cdot Ca_D, Ca_D \geq 0.187 \end{cases} \tag{31}$$

2.2.5.3. Calculation of the species transport and the electrochemistry. The next step consisted of simulating the coupled species transport and electrochemistry with a steady-state solver. A specific concentration of species i was considered in the Ω_1 subdomain (internal phase) and at the interface, while null concentration was specified in the subdomain Ω_2 (external phase). The species i dissolved in the subdomain Ω_2 reacted at the anode's surface following a concentration-dependent kinetics. Periodicity was ensured, as indicated in section 2.2.1.

A half-cell approach was adopted, considering a varying positive voltage at the anode ($+3$ V to $+4$ V in intervals of 0.1 V) while keeping 0 V at the cathode. E_{eq} was specified as 0 V and $+2.9$ V at the cathode and the anode, respectively. Moreover, the exchange current density was defined as $i_0 = 1.0$ A·m^{-2} at the anode, while $i_0 = 10$ A·m^{-2} was considered at the cathode.

The concentration of the species i transferred from the phase Ω_1 to phase Ω_2, the electrical conductivity ratio $\theta = \sigma_1/\sigma_2$ and the diffusivity of species i were systematically varied in the simulations:

- $c_{i,\Omega_1} = c_{i,int}$ assumed the values 500 mol·m^{-3}, 5 mol·m^{-3}, 0.5 mol·m^{-3}, and 0.05 mol·m^{-3}.
- θ was defined as 2 (500 μS·cm^{-1}/250 μS·cm^{-1}), 50 (500 μS·cm^{-1}/10 μS·cm^{-1}), 0.5 (250 μS·cm^{-1}/500 μS·cm^{-1}) and $\sim$ 0 (10^{-6} μS·cm^{-1}/250 μS·cm^{-1}).
- D_i was equal to 10^{-9} m^2·s^{-1} (reference), 10^{-8} m^2·s^{-1} and 10^{-10} m^2·s^{-1}.

2.2.5.4. CFD code and numerical details. The mathematical model was solved with the finite element method-based software COMSOL® Multiphysics (Burlington, MA), using the laminar flow, secondary current distribution and transport of diluted species modules. A mesh independence study was carried out to determine the optimal refinement level (i.e., capturing the intrinsic phenomena with an adequate computational cost). The optimal mesh refinement level consisted of $\sim$ 2.6 × 10^5 elements. The fluid flow (time-dependent) and the coupled mass transfer and electrochemistry (steady-state) were solved in two separate steps with direct solvers (MUMPS and PARDISO, respectively). The BDF algorithm was used for the variable time-stepping when solving the fluid dynamics.

3. Results and discussion

3.1. Fluid dynamics in the electrochemical microreactor

Fig. 3A presents the Taylor recirculation obtained through the CFD simulations in the 2D unit cell. The toroidal recirculation pattern obtained herein is consistent with previous works reported in the literature [58,63,88,89].
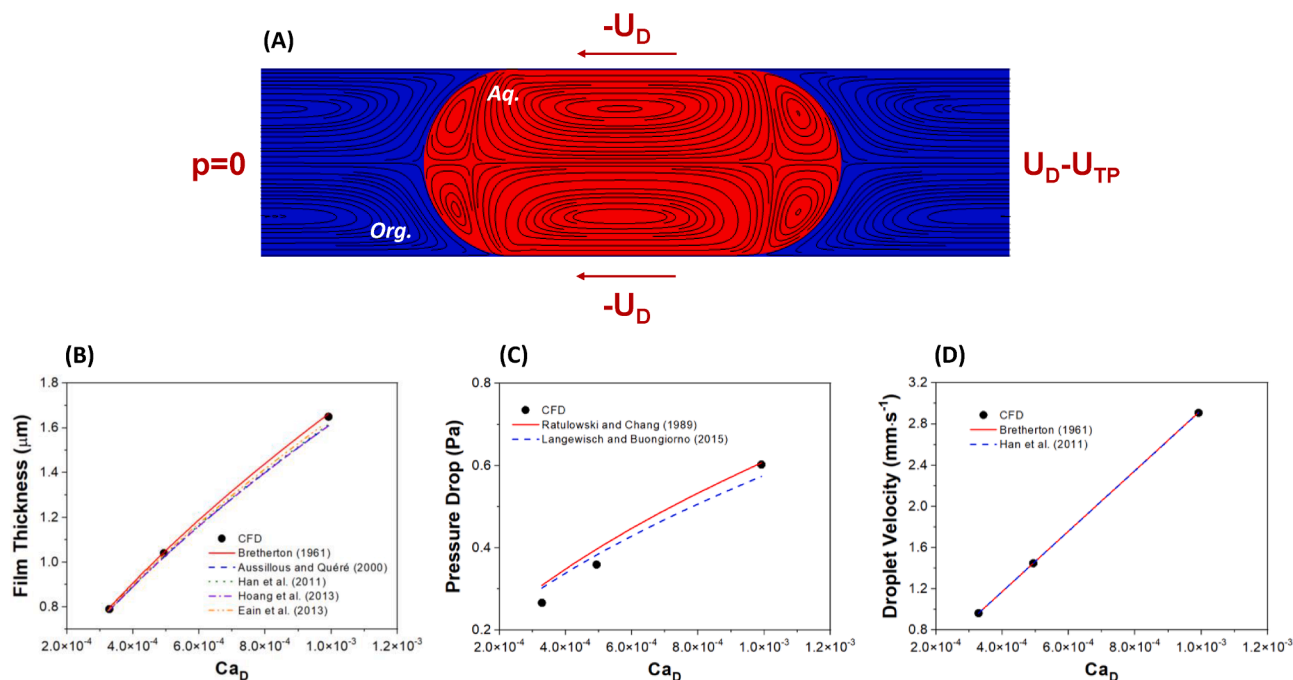
Fig. 3. (A) Taylor flow in the unit cell. (B) Film thickness as a function of the capillary number. (C) Pressure drop per droplet as a function of the capillary number. (D) Droplet velocity as a function of the capillary number.

In fact, Taylor recirculation plays a significant role in segmented flow in microchannels, contributing to intensifying the mixing [90]. Figures S1 and S2 illustrate the mixing occurring in the internal (Ω_1) and external (Ω_2) phases due to the recirculation found in this flow pattern. More details can be found in the Supplementary Information.

The reliability of the fluid dynamics model was tested in the 2D rectangular channel taking the external phase (Ω_2) film thickness, the droplet (internal phase, Ω_1) velocity and the pressure drop per droplet (internal phase, Ω_1) as reference. For the given set of boundary conditions specified, the wall velocity was iteratively varied until a steady-state was reached with stagnant internal phase (Ω_1) positioned at the UC's center (considering $\gamma = 0.5$ and $L_{UC} = 4H_{UC}$). Under these conditions, the thin film thickness was measured (average value in the uniform liquid film zone) and compared to the correlations expressed by Eqs. (25) to (28). Fig. 3B presents the external phase thin film thickness obtained numerically (CFD solution) and through the correlations of Bretherton [81], Aussillous and Quéré [82], Han, Shikazono and Kasagi [83] and Eain, Egan and Punch [84]. Good agreement was observed between the CFD results and all the correlations tested. The correlations from Aussillous and Queré, Han, Shikazono and Ksagi (HSK) and Eain, Egan and Punch (EEP) tended to underpredict the film thickness as the capillary number increased, while Bretherton's correlation resulted in a slight overprediction of δ for the higher capillary number evaluated.

A critical capillary number for the transition from viscous-capillary to viscous-inertial regime can be estimated as $Ca^* \sim \left(\mu^2/\rho R\sigma\right)^{3/4}$ [82,84]. For the conditions evaluated in this work, $Ca^* \sim 2.5$. Therefore, a viscous-capillary regime can be considered for all scenarios studied herein.

The theoretical expression proposed by Bretherton [81] ($10^{-4} < Ca < 10^{-2}$, inviscid gas bubbles, $\delta \ll R$) and the semi-empirical correlation presented by Aussillous and Quéré [82] ($Ca_b < 1.4$) were obtained for gas–liquid Taylor flow in circular channels. The model from Aussillous and Queré captures the capillary's confinement effect imposing a limit to the film thickness for large Ca_b, but reduces to Bretherton's predictions for low Ca_b. The correlations proposed by Bretherton and Aussillous and Quéré fail to capture inertial effects on the film thickness. The correlation proposed by Eain, Egan and Punch

[84] consists in a modification of the empirical coefficient in the expression from Aussillous and Quéré and considers liquid–liquid Taylor flow in circular channels ($Ca < 0.14$). The correlation of Han, Shikazono and Kasagi [83] is applicable for gas–liquid Taylor flow in between two parallel plates (considering $0 < Ca_b \lesssim 0.4$ and $Re < 2 \times 10^3$). Thus, it is suitable for the 2D cases evaluated in this work. Moreover, it accounts for the inertial effects (inertial thinning at low Re and inertial thickening at high Re) [87].

Therefore, given the low Ca_b and Re for the cases evaluated in this study, the film thickness obtained numerically is in good agreement with all correlations tested. Also, the low viscosity ratio for the internal/external phases (0.341) minimizes the effect of the droplet viscosity on the film thickness, as observed in previous works [54,56,91,92], so that the predictions from the Bretherton's correlation are in agreement with the CFD results.

It is also interesting to note, from Fig. 3C, that a good agreement was obtained when comparing the pressure drop per droplet (internal phase, Ω_1) and the prediction from the expressions proposed by Ratulowski and Chang [86] ($Ca_b < 10^{-1}$) and Langewisch and Buongiorno [87] ($Ca_b < 0.187$ and $Re < 5$). Finally, Fig. 3D shows that an excellent agreement was observed when comparing the droplet velocity obtained numerically (based on the iterative approach described earlier) and that predicted by Eq. (29) taking the film thickness predicted by the correlations of Bretherton [81] and Han, Shikazono and Kasagi [83] as reference.

It is important to highlight that different surface tension coefficients (taken as 1 mN·m^{-1} as a reference in this study) would essentially result in different thin film thicknesses.

In a previous study [41], we have simulated gas–liquid Taylor flow in microchannel electrochemical reactors in steady-state, considering that the shear rate at the interface is negligible. Therefore, the perfect slip boundary condition can be successfully applied to the interface. Since in liquid–liquid flow this assumption is not valid, the model must account for the shear rate at the interface. Thus, a proper boundary condition should be implemented at the interface, allowing for a steady-state solution similar to what we did in [41], or a multiphase model can be solved, which is the case of the moving mesh ALE approach used herein.

Robust results could also be obtained with traditional multiphase models, such as level-set, phase field, etc.

3.2. Liquid-liquid micro-flow electrochemistry

3.2.1. Polarization plots for the standard UC, considering different $c_{i,sat}$, D_i and β, for a given $\sigma_{\Omega_1}/\sigma_{\Omega_2}$

Fig. 4 presents the polarization plot (average current density measured at the anode varying the potential applied to the electrochemical cell in the range $+3$ V to $+4$ V in intervals of $+0.1$ V) for the standard UC, considering different concentrations ($c_{i,sat} = 500$ mol·m^{-3}, 5 mol·m^{-3}, 0.5 mol·m^{-3} and 0.05 mol·m^{-3}), diffusivities ($D_i = 10^{-8}$ m^2·s^{-1}, 10^{-9} m^2·s^{-1} and 10^{-10} m^2·s^{-1}) and velocities ($\beta = 1 - 3$), but keeping the internal:external phase electrical conductivity ratio as 2 (500 μS·cm^{-1} and 250 μS·cm^{-1} for the internal and external phase, respectively). Each row indicates a different diffusivity (10^{-8} m^2·s^{-1} → 10^{-10} m^2·s^{-1}), while each column represents a different velocity for a variable-length reactor ($\beta = 1 \rightarrow 3$).

3.2.1.1. Effect of $c_{i,sat}$, D_i and β, for a given $\sigma_{\Omega_1}/\sigma_{\Omega_2}$, on the performance of the electrochemical microreactor.
Overall, the diffusivity has a more significant effect on the reactor performance than the velocity. Concentrations higher than 500 mol·m^{-3} did not result in mass transfer limitations for any diffusivity or velocity tested. In fact, for 5 mol·m^{-3} the mass transfer limitations are negligible for all scenarios when considering $D_i = 10^{-8}$ m^2·s^{-1}. However, for $c_{i,sat} < 5$ mol·m^{-3}

significant mass transfer limitations can be observed for all velocities considered.

When the diffusivity $D_i = 10^{-9}$ m^2·s^{-1} is considered, mass transfer limitations have a weak but noticeable effect for 5 mol·m^{-3}. However, the higher the velocity, the lower these limitations, which is aligned with the expected behavior. A limiting current density can be observed for the lower concentration tested (0.05 mol·m^{-3}), indicating severe mass transfer limitations.

For the diffusivity $D_i = 10^{-10}$ m^2·s^{-1}, significant mass transfer limitations are observed for 5 mol·m^{-3} and a limiting current density is noticed even for 0.5 mol·m^{-3}.

Interestingly, lower velocities result in higher current densities saturation values (limiting current densities) for lower concentrations. As the velocity increases, the mixing effect due to the Taylor recirculation is more pronounced. As in Fig. S3A, it leads to a higher concentration gradient (dc_i/dH) close to the anode's surface at the midpoint of two consecutive droplets (considering the saturation concentration of 0.05 mol·m^{-3} of species i from the aqueous phase). At this point, a higher velocity results in a higher local species concentration at the anode's surface and a higher species flux towards the anode.

However, Fig. S3B shows that the concentration gradient (dc_i/dH) decreases as the velocity increases in the region of the external phase liquid film. In particular, this profile was obtained at the center of the liquid film region. Also, note that in this plot the concentration is represented across the entire thickness of the external phase liquid film, i.e., in between the liquid–liquid interface and the electrode (anode). The
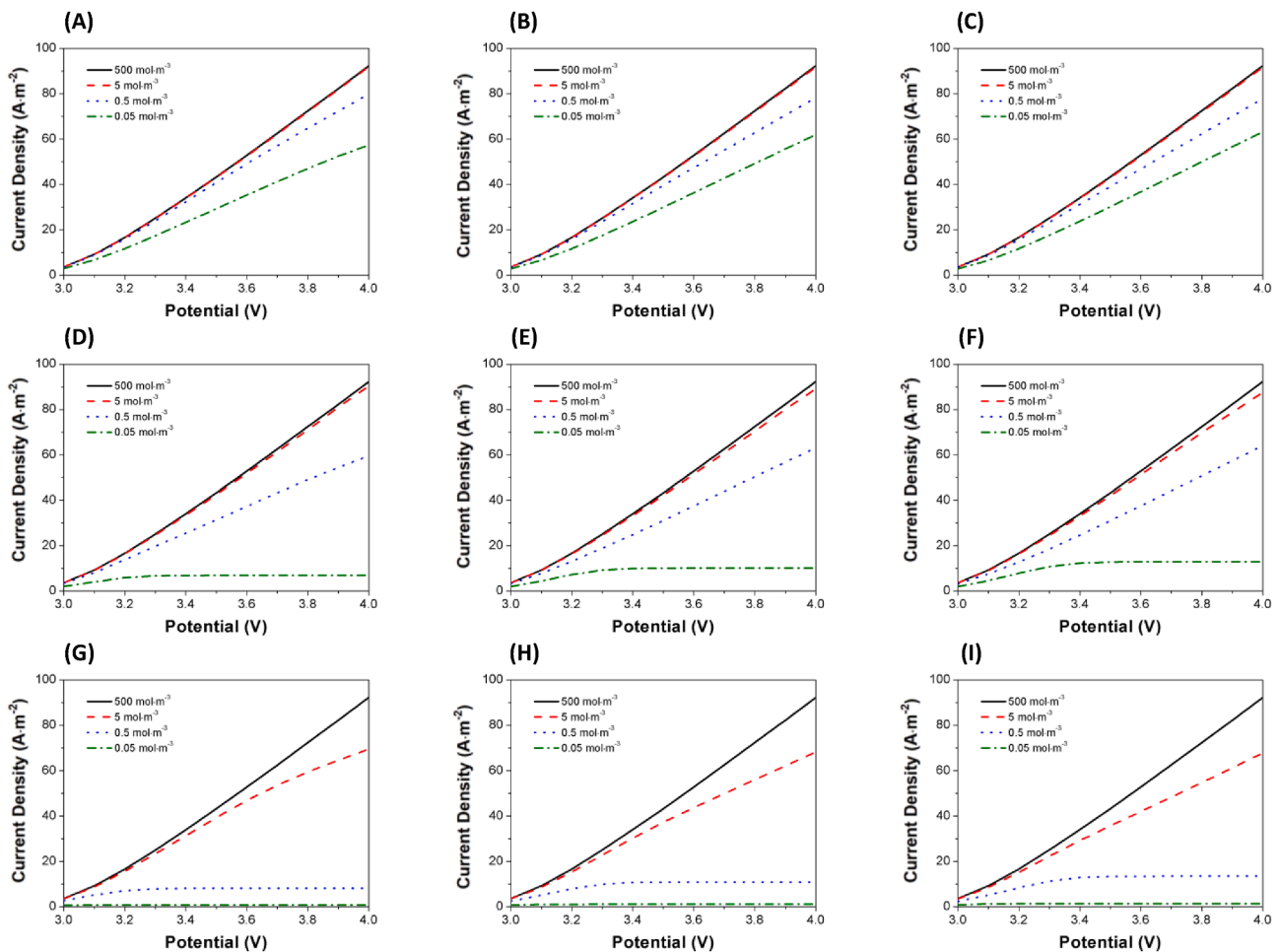

Fig. 4. Polarization plot. Each column represents a given velocity ($\beta = 3 \rightarrow 1$), while each row represents a diffusivity ($D_i = 10^{-8}$ m^2·s^{-1}), $D_i = 10^{-9}$ m^2·s^{-1} and $D_i = 10^{-10}$ m^2·s^{-1}, respectively). (A) $\beta = 3$, $D_i = 10^{-8}$ m^2·s^{-1}. (B) $\beta = 2$, $D_i = 10^{-8}$ m^2·s^{-1}. (C) $\beta = 1$, $D_i = 10^{-8}$ m^2·s^{-1}. (D) $\beta = 3$, $D_i = 10^{-9}$ m^2·s^{-1}. (E) $\beta = 2$, $D_i = 10^{-9}$ m^2·s^{-1}. (F) $\beta = 1$, $D_i = 10^{-9}$ m^2·s^{-1}. (G) $\beta = 3$, $D_i = 10^{-10}$ m^2·s^{-1}. (H) $\beta = 2$, $D_i = 10^{-10}$ m^2·s^{-1}. (I) $\beta = 1$, $D_i = 10^{-10}$ m^2·s^{-1}.

extent of this region (y-axis range) is naturally dependent on the velocity, as discussed in section 3.1. Thus, Fig. S3B reveals that the species flux to the anode decreases as the velocity increases. Moreover, the local concentration at the anode surface is lower for higher velocities. Overall, the average species mass flux to the anode increases as the velocity decreases, as illustrated in Fig. S3C.

Thus, the limiting current density obtained is higher for lower velocities than the higher velocities evaluated. Another important conclusion from Fig. S3C is that the higher mass flux in the UC occurs precisely at the dispersed phase region. Therefore, in systems where the electrical conductivity of the secondary phase is higher than that of the primary phase (e.g., in liquid–liquid processes operating with aqueous droplets in a continuous organic phase), there is an intensification of the reaction rate due to the presence of the dispersed phase.

From these observations, it is clear that it is relevant to operate electrochemical microreactors at high concentrations (>5 mol·m^{-3} for $D_i \geq 10^{-9}$ m^2·s^{-1}; 500 mol·m^{-3} for $D_i \sim 10^{-10}$ m^2·s^{-1}) since it maximizes the current/voltage relation. However, an optimization is required since excessively high concentrations (>500 mol·m^{-3}) will not result in any efficiency gain. Moreover, too high concentrations are challenging in microreactors due to solubility limits and thus clogging can occur when e.g., the product is less soluble than the starting materials.

3.2.2. Potential balance under different operational conditions

A complementary understanding of the effect of the different operational variables studied herein can be obtained from Fig. 5, representing the relative importance of the ohmic (η_{ohm}), concentration (η_{conc}) and activation (at the anode, $\eta_{(+)}^{act}$, and the cathode, $\eta_{(-)}$) overpotentials, excluding the equilibrium potential, i.e., $\left[E_{cell} / \left(\sum_i \eta_i - E_{eq} \right) \right] \times 100$, on the cell potential, for $D_i = 10^{-9}$ m^2·s^{-1}.

3.2.2.1. Effect of c$_{i,sat}$ and β, for a given σ$_{\Omega_1}$/σ$_{\Omega_2}$ and D$_i$. Clearly, for the

higher concentration (500 mol·m^{-3}) there is a negligible effect of varying the velocity (decreasing $\beta = 3 \rightarrow 1$ for (A) → (I)). For 5 mol·m^{-3} there is a noticeable increase in the concentration overpotential as E_{cell} increases for lower velocities due to the lower mixing effect in this scenario. As the concentration is even lower (0.5 mol·m^{-3} and 0.05 mol·m^{-3}), the concentration overpotential (η_{conc}) becomes significant and represents the largest fraction of the cell potential when the applied potential is increased. However, it is interesting to note that for the lower concentration evaluated (0.05 mol·m^{-3}), the concentration overpotential decreased as the velocity decreased. On the other hand, the ohmic drop increased as the velocity decreased, which can be attributed to a reduced ion transport between the electrodes at decreasing velocities. The activation overpotentials at the anode and the cathode were virtually independent of the velocity. The same behavior can be noticed for the concentration of 0.5 mol·m^{-3}.

3.2.2.2. Effect of c$_{i,sat}$ under different D$_i$, for a given β. Fig. 6 shows the effect of the diffusivity of species i on the potential distribution in the electrochemical cell.

Clearly, for the higher concentration (500 mol·m^{-3}), the effect of varying the diffusivity on the potential distribution is insignificant within the considered E_{cell} range. However, this behavior changes as the concentration of species i in the dispersed phase decreases. In the limit scenario where the concentration is as low as 0.05 mol·m^{-3}, the potential distribution is indeed significantly dependent on the species i diffusivity. Notably, for the diffusivity $D_i = 10^{-10}$ m^2·s^{-1}, the applied E_{cell} is essentially distributed in concentration and anode activation overpotential. As the diffusivity increases, more relevant is the ohmic drop contribution and the cathode activation potential, accompanied by a remarkable decrease of the concentration overpotential. Interestingly, when taking the higher E_{cell} as a reference, the anode overpotential is virtually independent of the diffusivity.
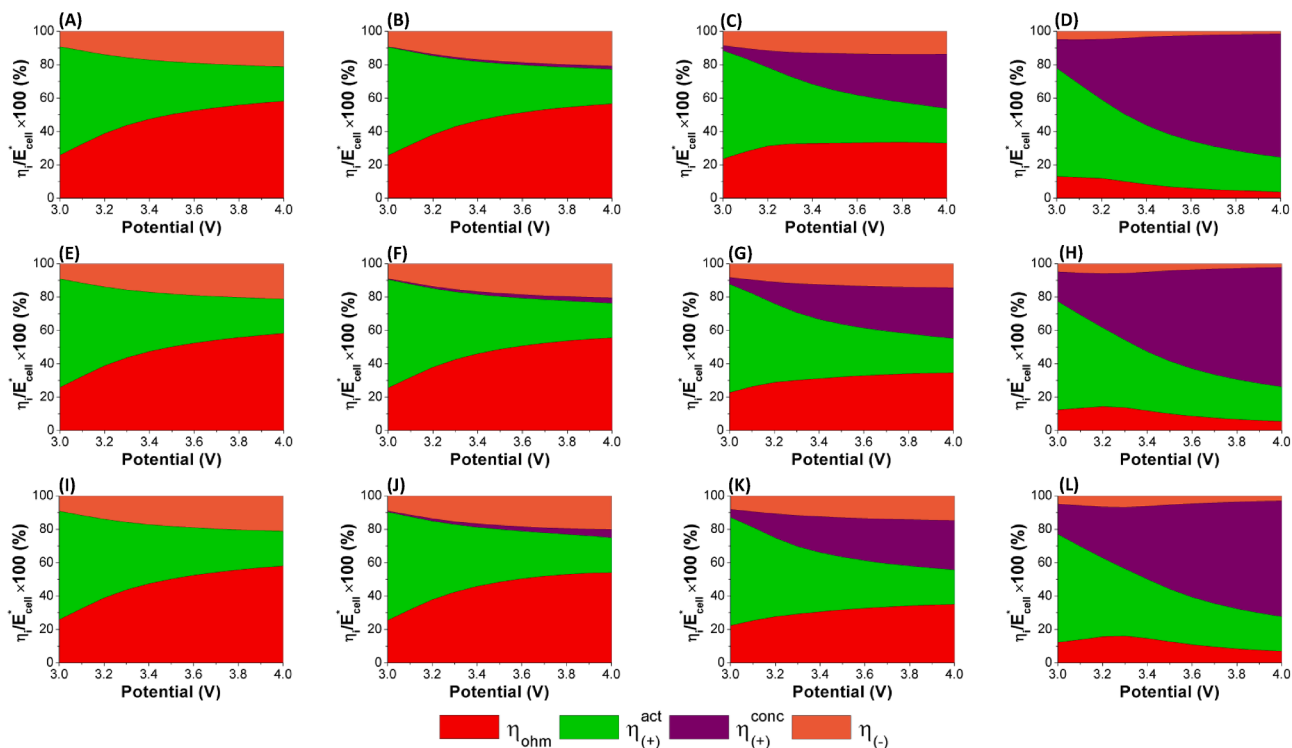

Fig. 5. Potential distribution map. Each column represents a concentration (500 mol·m^{-3}, 5 mol·m^{-3}, 0.5 mol·m^{-3} and 0.05 mol·m^{-3}, respectively), while each row represents a given velocity ($\beta = 3 \rightarrow 1$). $D_i = 10^{-9}$ m^2·s^{-1} in all cases. (A) $\beta = 3$, $c_{i,sat} = 500$ mol·m^{-3}. (B) $\beta = 3$, $c_{i,sat} = 5$ mol·m^{-3}. (C) $\beta = 3$, $c_{i,sat} = 0.5$ mol·m^{-3}. (D) $\beta = 3$, $c_{i,sat} = 0.05$ mol·m^{-3}. (E) $\beta = 2$, $c_{i,sat} = 500$ mol·m^{-3}. (F) $\beta = 2$, $c_{i,sat} = 5$ mol·m^{-3}. (G) $\beta = 2$, $c_{i,sat} = 0.5$ mol·m^{-3}. (H) $\beta = 2$, $c_{i,sat} = 0.05$ mol·m^{-3}. (I) $\beta = 1$, $c_{i,sat} = 500$ mol·m^{-3}. (J) $\beta = 1$, $c_{i,sat} = 5$ mol·m^{-3}. (K) $\beta = 1$, $c_{i,sat} = 0.5$ mol·m^{-3}. (L) $\beta = 1$, $c_{i,sat} = 0.05$ mol·m^{-3}.
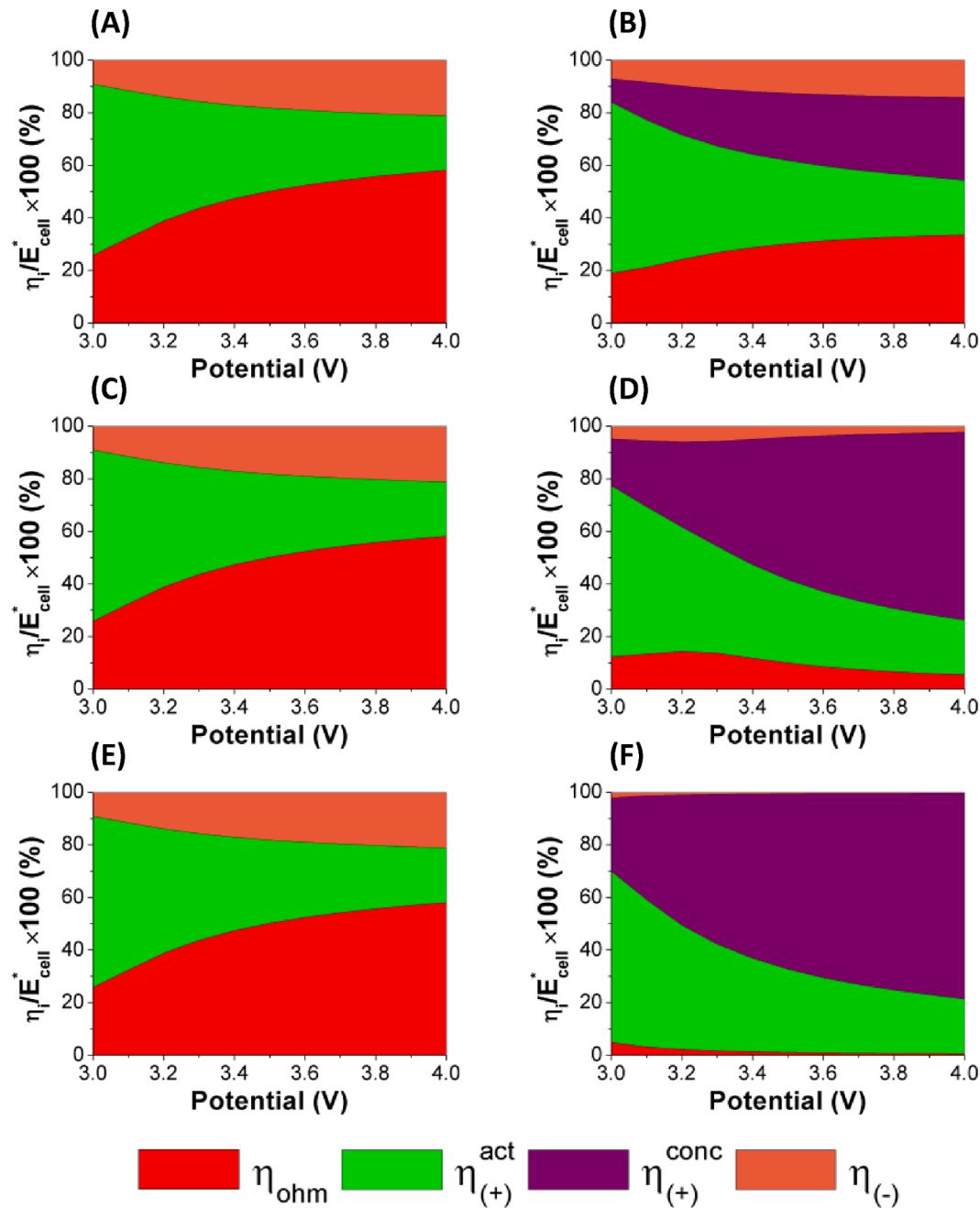
Fig. 6. Potential distribution map. First column represents the concentration of 500 mol·m^{-3}, while the second column represents the concentration of 0.05 mol·m^{-3} (i.e., the limits tested). Each row represents a different diffusivity ($D_i = 10^{-8}$ m^2·s^{-1}, $D_i = 10^{-9}$ m^2·s^{-1} and $D_i = 10^{-10}$ m^2·s^{-1}, respectively). (A) $D_i = 10^{-8}$ m^2·s^{-1}, $c_{i,sat} = 500$ mol·m^{-3}. (B) $D_i = 10^{-8}$ m^2·s^{-1}, $c_{i,sat} = 0.05$ mol·m^{-3}. (A) $D_i = 10^{-9}$ m^2·s^{-1}, $c_{i,sat} = 500$ mol·m^{-3}. (C) $D_i = 10^{-9}$ m^2·s^{-1}, $c_{i,sat} = 0.05$ mol·m^{-3}. (D) $D_i = 10^{-10}$ m^2·s^{-1}, $c_{i,sat} = 500$ mol·m^{-3}. (E) $D_i = 10^{-10}$ m^2·s^{-1}, $c_{i,sat} = 0.05$ mol·m^{-3}. $\beta = 2$ in all cases.

3.2.3. Polarization plot and potential balance for the effect of $c_{i,sat}$ under different $\sigma_{\Omega_1}/\sigma_{\Omega_2}$, for a given D_i and β

3.2.3.1. $\sigma_{\Omega 1}/\sigma_{\Omega 2} = 50$. Next, we set out to investigate the effect of the internal/external phase electrical conductivity ratio on the electrochemical performance. Fig. 7 shows the observed behavior when the electrical conductivity ratio was changed to 50 (500 μS·cm^{-1}:10 μS·cm^{-1} for the internal and external phase, respectively), keeping the diffusivity constant ($D_i = 10^{-9}$ m^2·s^{-1}) and considering the velocity multiplier $\beta = 2$.

In this scenario, the maximum current density observed (for the concentration of 500 mol·m^{-3}) is 55.6% lower than in the case where

$\sigma_{\Omega_1}/\sigma_{\Omega_2} = 2$. Moreover, it is interesting to note that for $\sigma_{\Omega_1}/\sigma_{\Omega_2} = 50$, the polarization curves overlap for the concentrations of 500 mol·m^{-3}, 5 mol·m^{-3} and 0.5 mol·m^{-3} (while for the reference case, $\sigma_{\Omega_1}/\sigma_{\Omega_2} = 2$, a deviation from the maximum current–voltage relation is observed for 0.5 mol·m^{-3}). A different behavior is observed for the concentration of 0.05 mol·m^{-3}, leading to a limiting current density. Interestingly, the limiting current density for $\sigma_{\Omega_1}/\sigma_{\Omega_2} = 50$ is virtually at the same level observed for $\sigma_{\Omega_1}/\sigma_{\Omega_2} = 2$. The potential distribution plot reveals that the ohmic drop effect dominates for the concentrations of 500 mol·m^{-3}, 5 mol·m^{-3} and 0.5 mol·m^{-3}. A small concentration overpotential is only observed when the concentration is reduced to 0.5 mol·m^{-3}. However, when the concentration is further reduced to 0.05 mol·m^{-3} the behavior is significantly different, and the concentration overpotential is the main

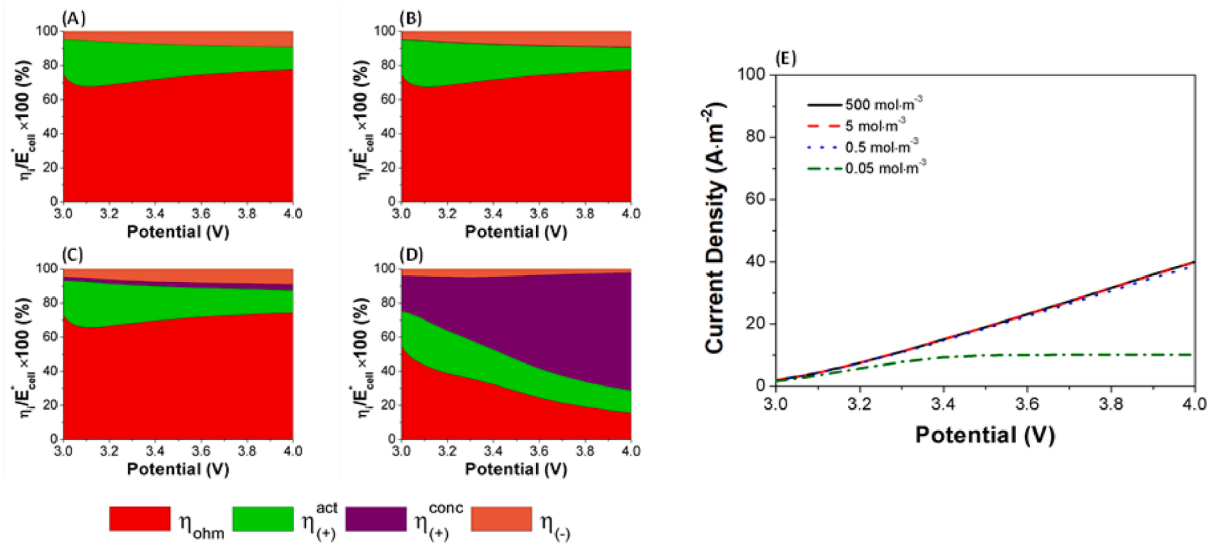**Fig. 7.** Potential distribution map and polarization plot for $\sigma_{\Omega_1}/\sigma_{\Omega_2} = 50$ (500 μS·cm^{-1}:10 μS·cm^{-1} for the internal and external phase, respectively), keeping $D_i = 10^{-9}$ m^2·s^{-1} and $\beta = 2$ in all cases. (A) – (D) illustrates the potential distribution for the concentrations of 500 mol·m^{-3}, 5 mol·m^{-3}, 0.5 mol·m^{-3} and 0.05 mol·m^{-3}, respectively, while (E) illustrates the polarization plot for different concentrations considering the E_{cell} range of 3 V – 4 V.

contributor as the E_{cell} is increased (although for $E_{cell} \rightarrow 3$ V the ohmic drop is still the controlling mechanism).

3.2.3.2. $\sigma_{\Omega_1}/\sigma_{\Omega_2} = 0.5$. Next, we have inverted the electrical conductivity ratio to $\sigma_{\Omega_1}/\sigma_{\Omega_2} = 0.5$ (250 μS·cm^{-1}:500 μS·cm^{-1} for the internal and external phase, respectively), keeping the diffusivity $D_i = 10^{-9}$ m^2·s^{-1} and $\beta = 2$. The results are summarized in Fig. 8.

In this scenario, the maximum current density for the concentration of 500 mol·m^{-3} is the same obtained in the reference case ($\sigma_{\Omega_1}/\sigma_{\Omega_2} = 2$). However, as the concentration is reduced, lower current densities are obtained as E_{cell} is increased for $\sigma_{\Omega_1}/\sigma_{\Omega_2} = 0.5$, but a limiting current density at the same level for $\sigma_{\Omega_1}/\sigma_{\Omega_2} = 2$ is observed when the lower concentration (0.05 mol·m^{-3}) is taken into account (i.e., the limits are kept constant, although some deviation occurs within the range analyzed). In terms of potential distribution, it is interesting to note that the ohmic drop dominates for the higher concentration (500 mol·m^{-3}) as E_{cell} increases. But, as $E_{cell} \rightarrow 3$ V, the anode activation overpotential becomes the dominating mechanism. Reducing the concentration has a

sensible impact on the potential distribution from 5 mol·m^{-3}, as the concentration overpotential is significant for $E_{cell} \rightarrow 4$ V. As the concentration is reduced to the lowest level tested (0.05 mol·m^{-3}), the concentration overpotential dominates the potential distribution in the electrochemical cell as $E_{cell} \rightarrow 4$ V. However, for $E_{cell} \rightarrow 3$ V the anode activation overpotential is the main mechanism. It is also interesting to note that the ohmic drop represents a smaller portion of the potential map in all conditions tested for $\sigma_{\Omega_1}/\sigma_{\Omega_2} = 0.5$ when compared to $\sigma_{\Omega_1}/\sigma_{\Omega_2} = 2$ (reference case).

3.2.3.3. $\sigma_{\Omega_1}/\sigma_{\Omega_2} \approx 10^{-9}$. Then, we investigated the scenario where $\sigma_{\Omega_1}/\sigma_{\Omega_2} \approx 10^{-9}$ (10^{-6} μS·cm^{-1}:500 μS·cm^{-1} for the internal and external phase, respectively), keeping the diffusivity $D_i = 10^{-9}$ m^2·s^{-1} and $\beta = 2$. This scenario corresponds to a limiting case where the electrical resistance in the internal phase tends to infinite. We have investigated it deeply in our previous study on the influence of gas–liquid segmented flow on the electrochemical performance [41]. Fig. 9 summarizes the results obtained.
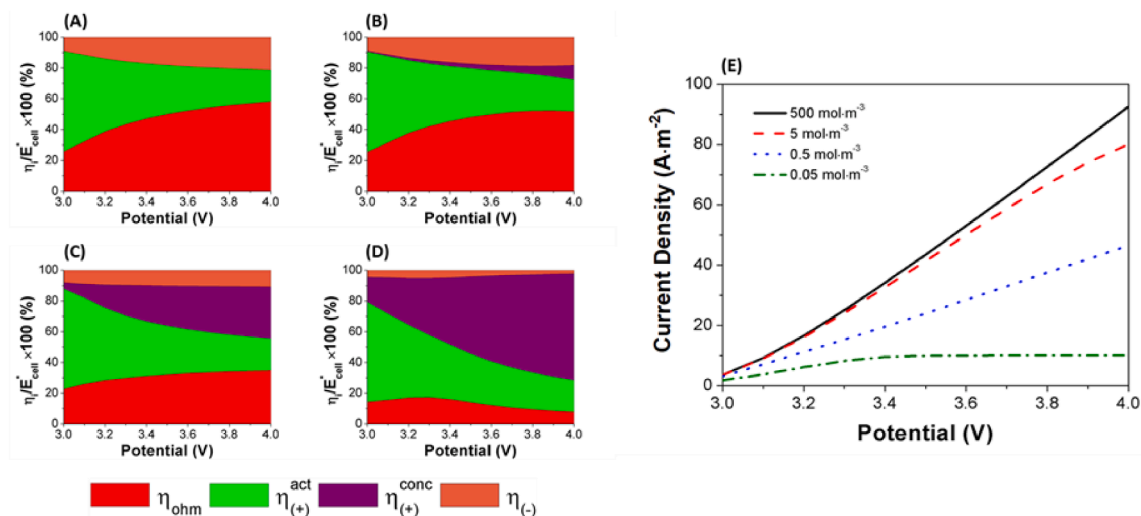
Fig. 8. Potential distribution map and polarization plot for $\sigma_{\Omega_1}/\sigma_{\Omega_2} = 0.5$ (250 μS·cm^{-1}:500 μS·cm^{-1} for the internal and external phase, respectively), keeping $D_i = 10^{-9}$ m^2·s^{-1} and $\beta = 2$ in all cases. (A) – (D) illustrates the potential distribution for the concentrations of 500 mol·m^{-3}, 5 mol·m^{-3}, 0.5 mol·m^{-3} and 0.05 mol·m^{-3}, respectively, while (E) illustrates the polarization plot for different concentrations considering the E_{cell} range of 3 V – 4 V.
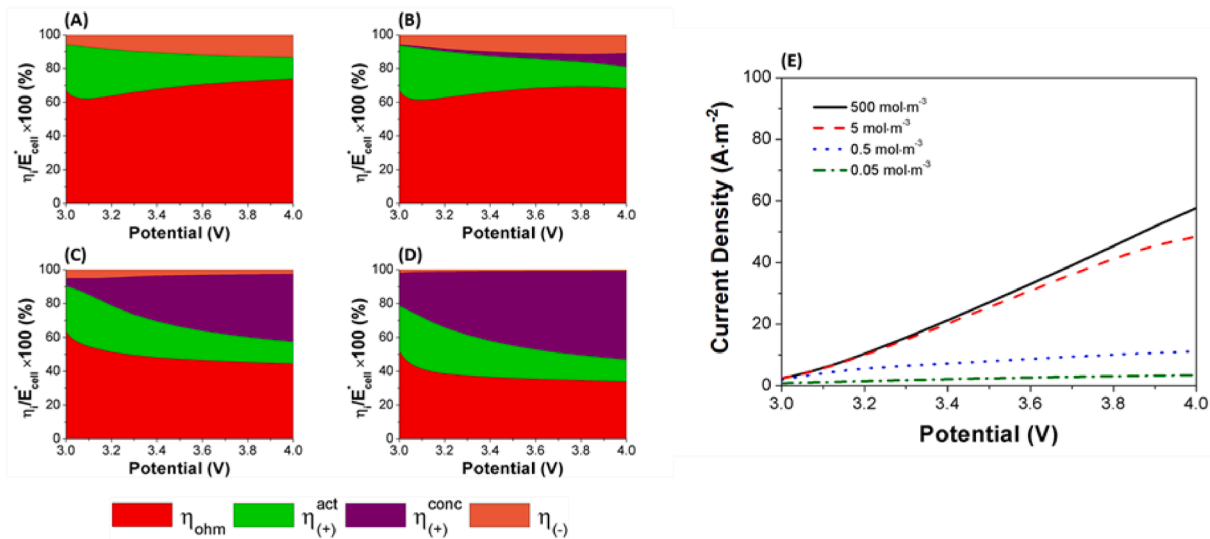
Fig. 9. Potential distribution map and polarization plot for $\sigma_{\Omega_1}/\sigma_{\Omega_2} \approx 10^{-9}$ (10^{-6} μS·cm^{-1}:500 μS·cm^{-1} for the internal and external phase, respectively), keeping $D_i = 10^{-9}$ m^2·s^{-1} and $\beta = 2$ in all cases. (A) – (D) illustrates the potential distribution for the concentrations of 500 mol·m^{-3}, 5 mol·m^{-3}, 0.5 mol·m^{-3} and 0.05 mol·m^{-3}, respectively, while (E) illustrates the polarization plot for different concentrations considering the E_{cell} range of 3 V – 4 V.

Overall, lower current densities were observed for all concentrations (500 mol·m^{-3}, 5 mol·m^{-3}, 0.5 mol·m^{-3} and 0.05 mol·m^{-3}). A reduction of approximately 34% is noticed for the higher concentration at the higher potential (4 V) when compared to the reference case ($\sigma_{\Omega_1}/\sigma_{\Omega_2} = 2$). Limiting current densities are observed for the concentrations of 0.5 mol·m^{-3} and 0.05 mol·m^{-3}. Interestingly, the plateau obtained for the concentration of 0.05 mol·m^{-3} is lower than the result obtained in the reference case.

Figure S4 illustrates the flux behavior for the electrochemical reactor operating with $\sigma_{\Omega_1}/\sigma_{\Omega_2} \approx 10^{-9}$. The reaction shuts down in the region of the internal phase. For the higher concentration tested (500 mol·m^{-3}), this scenario is even more noticeable. On the other hand, for the lower concentration (0.05 mol·m^{-3}), the species i flux is maximum at the edges of the internal phase.
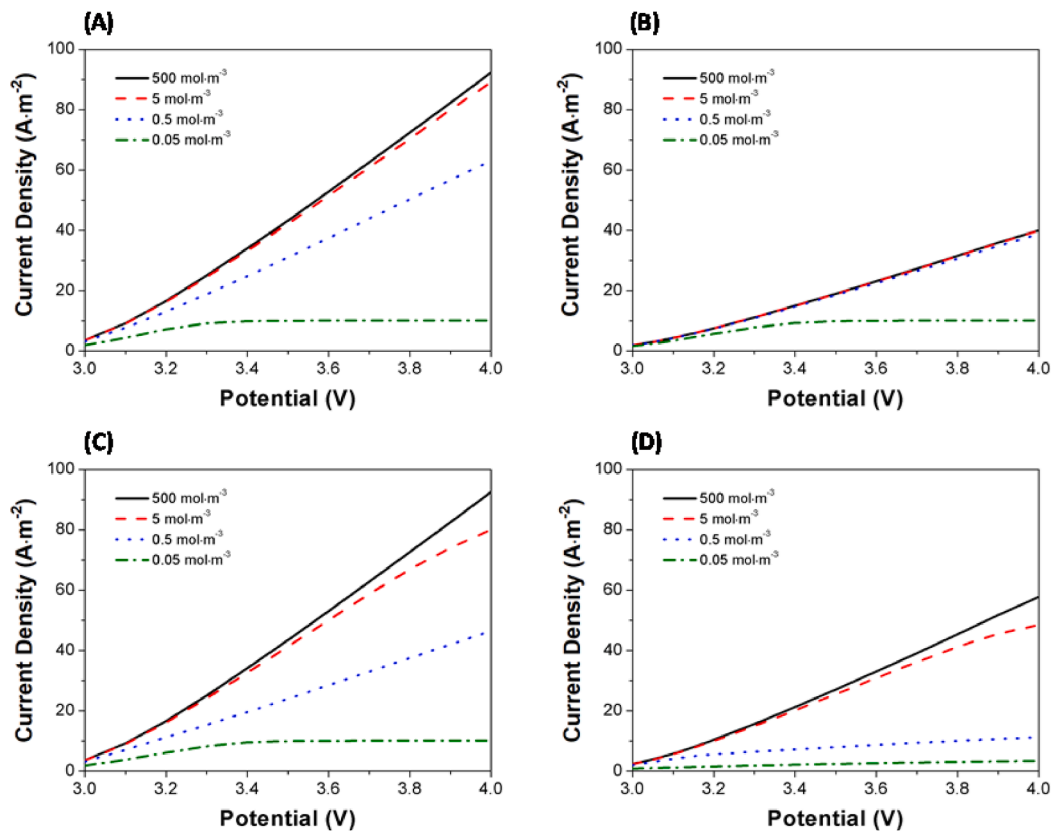
Fig. 10. Polarization plot for different operating conditions. (A) $\sigma_{\Omega_1}/\sigma_{\Omega_2} = 2$ (500 μS·cm^{-1}:250 μS·cm^{-1} for the internal and external phase, respectively). (B) $\sigma_{\Omega_1}/\sigma_{\Omega_2} = 50$ (500 μS·cm^{-1}:10 μS·cm^{-1} for the internal and external phase, respectively). (C) $\sigma_{\Omega_1}/\sigma_{\Omega_2} = 0.5$ (250 μS·cm^{-1}:500 μS·cm^{-1} for the internal and external phase, respectively). (D) $\sigma_{\Omega_1}/\sigma_{\Omega_2} \approx 10^{-9}$ (10^{-6} μS·cm^{-1}:500 μS·cm^{-1} for the internal and external phase, respectively). $D_i = 10^{-9}$ m^2·s^{-1} and $\beta = 2$ in all cases.

3.2.3.4. Summary of the effect of $c_{i,sat}$ under different $\sigma_{\Omega_1}/\sigma_{\Omega_2}$, for a given D_i and β, based on polarization plot. Fig. 10 summarizes the conclusions extracted from the study of the effect of the electrical conductivity ratio $\sigma_{\Omega_1}/\sigma_{\Omega_2}$ on the performance of the electrochemical reactor, based on the polarization plots. A higher $\sigma_{\Omega_2}/\sigma_{\Omega_1}$ leads to better performance. However, for optimal operation, σ_{Ω_2} must be tuned to significant levels, as lower values for this parameter are detrimental for the overall performance. While the reaction is intensified at the internal phase region when $\sigma_{\Omega_1} > \sigma_{\Omega_2}$, the reaction shuts down in this region when $\sigma_{\Omega_1}/\sigma_{\Omega_2} \to 0$, i.e., when the electrical resistance in the internal phase becomes almost infinite; this is a situation which is comparable to gas–liquid Taylor flow where no ion transport is observed in the gas bubble region.

3.2.4. Polarization plot and potential balance for the effect of $c_{i,sat}$ and γ, for a given D_i, β and $\sigma_{\Omega_1}/\sigma_{\Omega_2}$

Finally, we investigated the effect of different configurations for the UC, considering a varying γ (volume fraction ratio of internal/external phase) first. As γ is reduced for the same set of operational conditions (diffusivity $D_i = 10^{-9}$ m^2·s^{-1}, $\beta = 2$ and $\sigma_{\Omega_1}/\sigma_{\Omega_2} = 2$) the reactor performance deteriorates. With lower γ, the current density is lower for a given E_{cell}. While for the higher concentration tested (500 mol·m^{-3}) the potential distribution is virtually independent of γ, this scenario is different when the concentration of 0.05 mol·m^{-3} is considered. In this case, as γ is reduced, the ohmic drop reduces and the concentration overpotential increases, becoming the dominating mechanism as $E_{cell} \to 4$ V. Therefore, it is preferable to operate the reactor with a higher frequency of dispersed phase to maximize its performance. Fig. 11 illustrates this behavior.

3.2.5. Complementary studies about the effect of relevant varibles on the performance of electrochemical microreactors

The effect of increasing the UC length while keeping the volume fraction of the internal phase (γ) constant (i.e., working with elongated internal phase), varying the inter-electrode gap (H) as well as the maps for the electrolyte potential, electrolyte current density and concentration for the system operating under different reaction conditions are presented and discussed in the Supplementary Information.

3.2.6. Electrolyte potential, electrolyte current density and concentration maps

Figs. 12 and 13 illustrate the electrolyte potential, electrolyte current density and concentration maps for the system operating under different reaction conditions. In Fig. 12, one can notice that for $\sigma_{\Omega_1}/\sigma_{\Omega_2} = 2$, $D_i = 10^{-9}$ m^2·s^{-1} and $\beta = 2$, i.e., the standard case for a concentration of 500 mol·m^{-3}, it is clear to see the intensification of the reaction rate at the region of the internal phase, regardless of E_{cell}.

It is also interesting to note that as the diffusivity decreases, the reactor tends to operate like a divided cell, as shown in Figure S7. Moreover, Fig. 13 presents the behavior when the conditions from Fig. 12 are kept constant, but the concentration is reduced to the lower limit (0.05 mol·m^{-3}). Clearly, in this scenario there is still an intensification of the reaction rate at the region of the internal phase, but the pattern observed for the electrolyte potential and the electrolyte current density is significantly different.
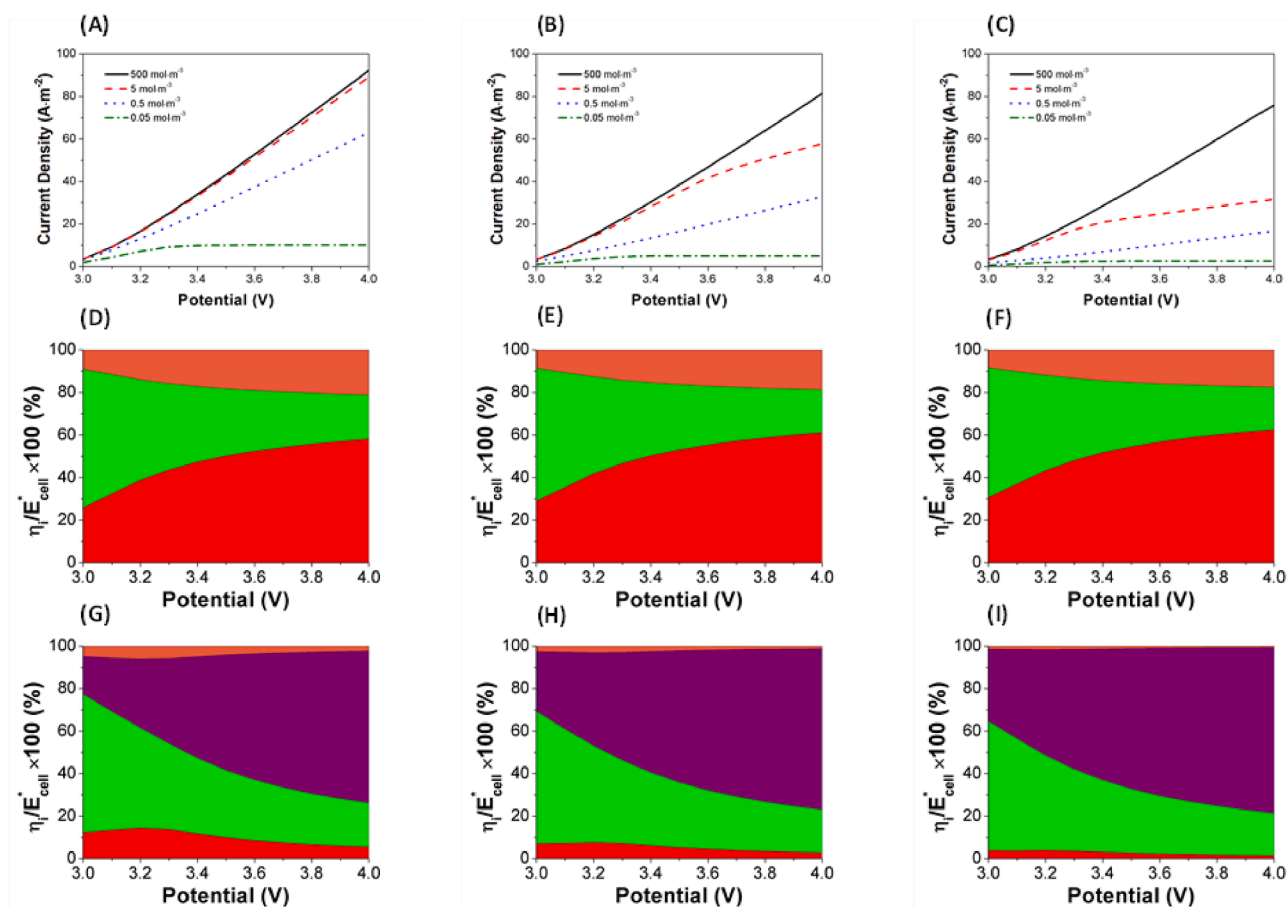
Fig. 11. Polarization plot and potential distribution map as a function of the volume fraction (γ) of the internal phase and the concentration. Each column represents a different volume fraction ($\gamma = 0.5$, $\gamma = 0.25$ and $\gamma = 0.125$, respectively). Second row illustrates the behavior for the concentration of 500 mol·m^{-3}, while the third row represents the concentration of 0.05 mol·m^{-3} (i.e., the limits of analysis). $D_i = 10^{-9}$ m^2·s^{-1} and $\beta = 2$ in all cases.

Fig. 12. Contours of electrolyte potential, electrolyte current density and concentration as a function of the applied potential (E_{cell}), considering a concentration of 500 mol·m^{-3} in the internal phase. (A) Electrolyte potential for $E_{cell} = 3$ V. (B) Electrolyte potential for $E_{cell} = 4$ V. (C) Electrolyte current density for $E_{cell} = 3$ V. (D) Electrolyte current density for $E_{cell} = 4$ V. (E) Concentration for $E_{cell} = 3$ V. (F) Concentration for $E_{cell} = 4$ V. $D_i = 10^{-9}$ m^2·s^{-1}, $\beta = 2$ and $\sigma_{\Omega_1}/\sigma_{\Omega_2} = 2$ in all cases.
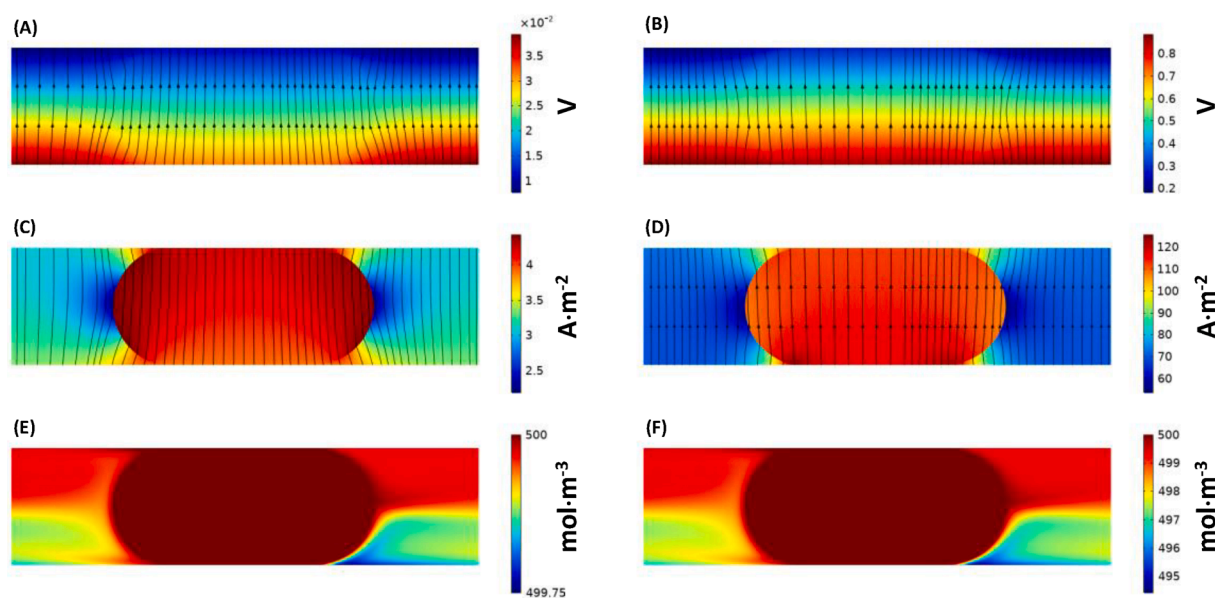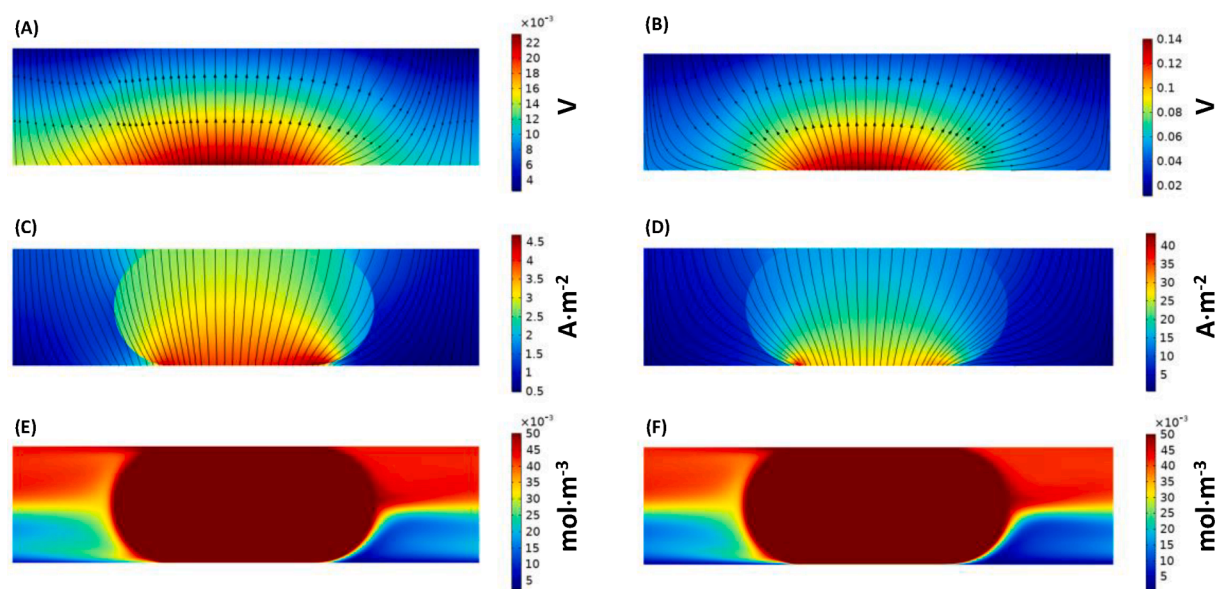

Fig. 13. Contours of electrolyte potential, electrolyte current density and concentration as a function of the applied potential (E_{cell}), considering a concentration of 0.05 mol·m^{-3} in the internal phase. (A) Electrolyte potential for for $E_{cell} = 3$ V. (B) Electrolyte potential for $E_{cell} = 4$ V. (C) Electrolyte current density for $E_{cell} = 3$ V. (D) Electrolyte current density for $E_{cell} = 4$ V. (E) Concentration for $E_{cell} = 3$ V. (F) Concentration for $E_{cell} = 4$ V. $D_i = 10^{-9}$ m^2·s^{-1}, $\beta = 2$ and $\sigma_{\Omega_1}/\sigma_{\Omega_2} = 2$ in all cases.

4. Conclusions

We have conducted a phenomenological investigation on the effect of different operational scenarios for liquid–liquid Taylor flow electrochemistry. We show that the selected variables (electrical conductivity ratio, mass diffusivity, velocity, concentration, cell potential, internal phase volume fraction, internal phase length and inter-electrode distance) have different impact levels on the reactor performance, with a strong interdependence.

Operating micro-flow electrochemical devices at high concentrations is beneficial in all scenarios evaluated. However, a large excess should be avoided as it does not result in a further improvement after a specific limit which should be optimized for each specific electrochemical

transformation and reactor configuration. Moreover, the systems take advantage of higher diffusivities, although even in this case, limiting current densities can be noticed when operating at low concentrations.

In all cases, operating with an electrical conductivity ratio > 1 for internal:external phase is beneficial, which is commonly observed when working with aqueous droplets in a continuous organic phase. In general, the higher the ratio, the better the performance. However, care should be taken to keep the external phase electrical conductivity at sufficiently high levels to ensure the improved performance. The velocity impact is significant only under specific operating windows, and in some cases working at lower velocities is beneficial since higher limiting current densities are observed (and consequently, the reaction rate is improved).

The higher the applied potential, the better the performance in terms of current density (and consequently reaction rate) at a given set of operating conditions. However, it should be noted that in some cases a limiting level is reached due to severe mass transfer limitations (null limiting reagent concentration at the working electrode surface). Interestingly, a diverse set of potential distribution fractions (considering ohmic, concentration and activation overpotentials) is observed as the cell potential is varied under the subspaces of independent variables.

The flow arrangement (internal phase volume fraction, droplet length and inter-electrode distance) also has a significant effect on the electrochemical performance, although the same limiting-behaviors can be observed in some scenarios.

Finally, we believe that the insights gained herein will be important to electrochemistry practitioners in both academia and industry to develop more efficient electrochemical micro-flow reactors and processes for liquid–liquid transformations.

Declaration of Competing Interest

The authors declare that they have no known competing financial interests or personal relationships that could have appeared to influence the work reported in this paper.

Acknowledgments

Appendix A. Supplementary data

Supplementary data to this article can be found online at https://doi.org/10.1016/j.cej.2021.131443.

References

[1] S.V. Mohan, R. Katakojwala, The circular chemistry conceptual framework: A way forward to sustainability in industry 4.0, Current Opinion in Green and Sustainable, Chemistry 28 (2021), 100434, https://doi.org/10.1016/j.cogsc.2020.100434.

[2] F. Yang, S. Gu, Industry 4.0, a revolution that requires technology and national strategies, Complex & Intelligent Systems 7(3) (2021) 1311-1325. https://doi.org/10.1007/s40747-020-00267-9.

[3] T. Van Gerven, A. Stankiewicz, Structure, Energy, Synergy, Time—The Fundamentals of Process Intensification, Ind. Eng. Chem. Res. 48 (5) (2009) 2465–2474, https://doi.org/10.1021/ie801501y.

[4] F.J. Keil, Process intensification, Rev. Chem. Eng. 34 (2) (2018) 135–200, https://doi.org/10.1515/revce-2017-0085.

[5] S. Becht, R. Franke, A. Geißelmann, H. Hahn, An industrial view of process intensification, Chem. Eng. Process. Process Intensif. 48 (1) (2009) 329–332, https://doi.org/10.1016/j.cep.2008.04.012.

[6] J.M. Ponce-Ortega, M.M. Al-Thubaiti, M.M. El-Halwagi, Process intensification: New understanding and systematic approach, Chem. Eng. Process. Process Intensif. 53 (2012) 63–75, https://doi.org/10.1016/j.cep.2017.08.013.

[7] D.F. Rivas, E. Castro-Hernández, A.L. Villanueva Perales, W. van der Meer, Evaluation method for process intensification alternatives, Chemical Engineering and Processing - Process Intensification (2018) 221–232, https://doi.org/10.1016/j.cep.2017.08.013.

[8] Y.-H. Kim, L.K. Park, S. Yiacoumi, C. Tsouris, Modular Chemical Process Intensification: A Review, Annual Review of Chemical and Biomolecular Engineering 8 (1) (2017) 359–380, https://doi.org/10.1146/annurev-chembioeng-060816-101354.

[9] D.C. Boffito, D. Fernandez Rivas, Process intensification connects scales and disciplines towards sustainability, The Canadian Journal of Chemical Engineering 98(12) (2020) 2489-2506. https://doi.org/10.1002/cjce.23871.

[10] F.M. Dautzenberg, M. Mukherjee, Process intensification using multifunctional reactors, Chem. Eng. Sci. 56 (2) (2001) 251–267, https://doi.org/10.1016/S0009-2509(00)00228-1.

[11] A. Chaudhuri, K.P.L. Kuijpers, R.B.J. Hendrix, P. Shivaprasad, J.A. Hacking, E.A. C. Emanuelsson, T. Noël, J. van der Schaaf, Process intensification of a photochemical oxidation reaction using a Rotor-Stator Spinning Disk Reactor: A strategy for scale up, Chem. Eng. J. 400 (2020), 125875, https://doi.org/10.1016/j.cej.2020.125875.

[12] Z. Dong, Z. Wen, F. Zhao, S. Kuhn, T. Noël, Scale-up of micro- and milli-reactors: An overview of strategies, design principles and applications, Chemical Engineering Science: X 10 (2021), 100097, https://doi.org/10.1016/j.cesx.2021.100097.

[13] S.P. Balomenou, D. Tsiplakides, A. Katsaounis, S. Brosda, A. Hammad, G. Fóti, C. Comninellis, S. Thiemann-Handler, B. Cramer, C.G. Vayenas, Monolithic electrochemically promoted reactors: A step for the practical utilization of electrochemical promotion, Solid State Ionics 177 (26) (2006) 2201–2204, https://doi.org/10.1016/j.ssi.2006.03.027.

[14] C. Wang, Y. Gu, S. Wu, H. Yu, S. Chen, Y. Su, Y. Guo, X. Wang, H. Chen, W. Kang, X. Quan, Construction of a Microchannel Electrochemical Reactor with a Monolithic Porous-Carbon Cathode for Adsorption and Degradation of Organic Pollutants in Several Minutes of Retention Time, Environ. Sci. Technol. 54 (3) (2020) 1920–1928, https://doi.org/10.1021/acs.est.9b06266.

[15] M.F. Rabuni, N. Vatcharasuwan, T. Li, K. Li, High performance micro-monolithic reversible solid oxide electrochemical reactor, J. Power Sources 458 (2020), 228026, https://doi.org/10.1016/j.jpowsour.2020.228026.

[16] V. Hessel, Novel Process Windows – Gates to Maximizing Process Intensification via Flow Chemistry, Chem. Eng. Technol. 32 (11) (2009) 1641–1642, https://doi.org/10.1002/ceat.200990054.

[17] V. Hessel, D. Kralisch, N. Kockmann, T. Noël, Q. Wang, Novel Process Windows for Enabling, Accelerating, and Uplifting Flow Chemistry, ChemSusChem 6 (5) (2013) 746–789, https://doi.org/10.1002/cssc.201200766.

[18] A. Hammad, S. Souentie, E.I. Papaioannou, S. Balomenou, D. Tsiplakides, J. C. Figueroa, C. Cavalca, C.J. Pereira, Electrochemical promotion of the SO2 oxidation over thin Pt films interfaced with YSZ in a monolithic electropromoted reactor, Appl. Catal. B 103 (3) (2011) 336–342, https://doi.org/10.1016/j.apcatb.2011.01.040.

[19] S. Balomenou, D. Tsiplakides, A. Katsaounis, S. Thiemann-Handler, B. Cramer, G. Foti, C. Comninellis, C.G. Vayenas, Novel monolithic electrochemically promoted catalytic reactor for environmentally important reactions, Appl. Catal. B 52 (3) (2004) 181–196, https://doi.org/10.1016/j.apcatb.2004.04.007.

[20] C. Chatzilias, E. Martino, A. Katsaounis, C.G. Vayenas, Electrochemical promotion of CO2 hydrogenation in a monolithic electrochemically promoted reactor (MEPR), Appl. Catal. B 284 (2021), 119695, https://doi.org/10.1016/j.apcatb.2020.119695.

[21] M. Jacobs, E. Kayahan, L.C.J. Thomassen, S. Kuhn, M.E. Leblebici, First generation of translucent monoliths for photochemical applications, Journal of Advanced Manufacturing and Processing 2 (2) (2020), e10047, https://doi.org/10.1002/amp2.10047.

[22] V. Tomašić, F. Jović, State-of-the-art in the monolithic catalysts/reactors, Appl. Catal. A 311 (2006) 112–121, https://doi.org/10.1016/j.apcata.2006.06.013.

[23] J.A. Moulijn, F. Kapteijn, Monolithic reactors in catalysis: excellent control, Curr. Opin. Chem. Eng. 2 (3) (2013) 346–353, https://doi.org/10.1016/j.coche.2013.05.003.

[24] Y. Su, N.J.W. Straathof, V. Hessel, T. Noël, Photochemical Transformations Accelerated in Continuous-Flow Reactors: Basic Concepts and Applications, Chemistry – A European Journal 20(34) (2014) 10562–10589, https://doi.org/10.1002/chem.201400283.

[25] C. Sambiagio, T. Noël, Flow photochemistry: Shine some light on those tubes!, Trends in Chemistry 2 (2) (2020) 92–106.

[26] T. Noël, Y. Cao, G. Laudadio, The Fundamentals Behind the Use of Flow Reactors in Electrochemistry, Acc. Chem. Res. 52 (10) (2019) 2858–2869, https://doi.org/10.1021/acs.accounts.9b00412.

[27] M. Atobe, H. Tateno, Y. Matsumura, Applications of Flow Microreactors in Electrosynthetic Processes, Chem. Rev. 118 (9) (2018) 4541–4572, https://doi.org/10.1021/acs.chemrev.7b00353.

[28] B. Obama, The irreversible momentum of clean energy, Science 355 (6321) (2017) 126–129.

[29] N. Armaroli, V. Balzani, Towards an electricity-powered world, Energy Environ. Sci. 4 (9) (2011) 3193–3222.

[30] N. Tanbouza, T. Ollevier, K. Lam, Bridging Lab and Industry with Flow Electrochemistry, Iscience (2020), 101720.

[31] M. Yan, Y. Kawamata, P.S. Baran, Synthetic organic electrochemical methods since 2000: on the verge of a renaissance, Chem. Rev. 117 (21) (2017) 13230–13319.

[32] A. Wiebe, T. Gieshoff, S. Möhle, E. Rodrigo, M. Zirbes, S.R. Waldvogel, Electrifying organic synthesis, Angew. Chem. Int. Ed. 57 (20) (2018) 5594–5619.

[33] F. Marken, J.D. Wadhawan, Multiphase methods in organic electrosynthesis, Acc. Chem. Res. 52 (12) (2019) 3325–3338.

[34] S. Tang, S. Liu, A. Lei, Electrochemical oxidative cross-coupling with hydrogen evolution: a green and sustainable way for bond formation, Chem 4 (1) (2018) 27–45.

[35] F. Reymond, D. Fermın, H.J. Lee, H.H. Girault, Electrochemistry at liquid/liquid interfaces: methodology and potential applications, Electrochim. Acta 45 (15–16) (2000) 2647–2662.

[36] F. Scholz, Recent advances in the electrochemistry of ion transfer processes at liquid–liquid interfaces, Annual Reports Section" C"(Physical Chemistry) 102 (2006) 43–70.

[37] P. Vanýsek, Charge transfer processes on liquid/liquid interfaces: the first century, Electrochim. Acta 40 (18) (1995) 2841–2847.

[38] R. Gupta, D. Fletcher, B. Haynes, Taylor flow in microchannels: a review of experimental and computational work, The Journal of Computational Multiphase Flows 2 (1) (2010) 1–31.

[39] S. Haase, D.Y. Murzin, T. Salmi, Review on hydrodynamics and mass transfer in minichannel wall reactors with gas–liquid Taylor flow, Chem. Eng. Res. Des. 113 (2016) 304–329.

[40] P. Sobieszuk, J. Aubin, R. Pohorecki, Hydrodynamics and mass transfer in gas-liquid flows in microreactors, Chem. Eng. Technol. 35 (8) (2012) 1346–1358.

[41] Y. Cao, C. Soares, N. Padoin, T. Noël, Gas bubbles have controversial effects on Taylor flow electrochemistry, Chem. Eng. J. 406 (2021), 126811.

[42] J.O. de Brito Lira, H.G. Riella, N. Padoin, C. Soares, An Overview of Photoreactors and Computational Modeling for the Intensification of Photocatalytic Processes in the Gas-Phase: State-of-Art, Journal of Environmental, Chem. Eng. (2021), 105068.

[43] J.O. Lira, H.G. Riella, N. Padoin, C. Soares, CFD+ DoE optimization of a flat plate photocatalytic reactor applied to NOx abatement, Chemical Engineering and Processing-Process Intensification 154 (2020), 107994.

[44] G.X. de Oliveira, J.O. Lira, D. Cambié, T. Noël, H.G. Riella, N. Padoin, C. Soares, CFD analysis of a luminescent solar concentrator-based photomicroreactor (LSC-PM) with feedforward control applied to the synthesis of chemicals under fluctuating light intensity, Chem. Eng. Res. Des. 153 (2020) 626–634.

[45] J. de OB Lira, N. Padoin, V.J. Vilar, C. Soares, Photocatalytic NOx abatement: Mathematical modeling CFD validation and reactor analysis, J. Hazard. Mater. 372 (2019) 145–153.

[46] N. Padoin, A.Z. de Souza, K. Ropelato, C. Soares, Numerical simulation of isothermal gas – liquid flow patterns in microchannels with varying wettability, Chem. Eng. Res. Des. 109 (2016) 698–706.

[47] N. Padoin, C. Soares, An explicit correlation for optimal TiO2 film thickness in immobilized photocatalytic reaction systems, Chem. Eng. J. 310 (2017) 381–388.

[48] N. Padoin, A.T. Dal'Toé, L.P. Rangel, K. Ropelato, C. Soares, Heat and mass transfer modeling for multicomponent multiphase flow with CFD, Int. J. Heat Mass Transf. 73 (2014) 239–249.

[49] D. Cambie, C. Bottecchia, N.J. Straathof, V. Hessel, T. Noel, Applications of continuous-flow photochemistry in organic synthesis, material science, and water treatment, Chem. Rev. 116 (17) (2016) 10276–10341.

[50] S.L. Poe, M.A. Cummings, M.P. Haaf, D.T. McQuade, Solving the Clogging Problem: Precipitate-Forming Reactions in Flow, Angew. Chem. 118 (10) (2006) 1574–1578.

[51] A. Karim, J. Bravo, D. Gorm, T. Conant, A. Datye, Comparison of wall-coated and packed-bed reactors for steam reforming of methanol, Catal. Today 110 (1–2) (2005) 86–91.

[52] V. Sebastian Cabeza, S. Kuhn, A.A. Kulkarni, K.F. Jensen, Size-controlled flow synthesis of gold nanoparticles using a segmented flow microfluidic platform, Langmuir 28 (17) (2012) 7007–7013.

[53] A. Günther, K.F. Jensen, Multiphase microfluidics: from flow characteristics to chemical and materials synthesis, Lab Chip 6 (12) (2006) 1487–1503.

[54] R. Gupta, S.S. Leung, R. Manica, D.F. Fletcher, B.S. Haynes, Hydrodynamics of liquid–liquid Taylor flow in microchannels, Chem. Eng. Sci. 92 (2013) 180–189.

[55] A. Abdollahi, S.E. Norris, R.N. Sharma, Pressure Drop and Film Thickness of Liquid-Liquid Taylor Flow in Square Microchannels, Int. J. Heat Mass Transf. 156 (2020), 119802.

[56] J. Jovanović, W. Zhou, E.V. Rebrov, T. Nijhuis, V. Hessel, J.C. Schouten, Liquid–liquid slug flow: hydrodynamics and pressure drop, Chem. Eng. Sci. 66 (1) (2011) 42–54.

[57] P. Desir, T.-Y. Chen, M. Bracconi, B. Saha, M. Maestri, D.G. Vlachos, Experiments and computations of microfluidic liquid–liquid flow patterns, React. Chem. Eng. 5 (1) (2020) 39–50.

[58] A. Abdollahi, S.E. Norris, R.N. Sharma, Fluid flow and heat transfer of liquid-liquid Taylor flow in square microchannels, Appl. Therm. Eng. 172 (2020), 115123.

[59] Z. Dai, Z. Guo, D.F. Fletcher, B.S. Haynes, Taylor flow heat transfer in microchannels—Unification of liquid–liquid and gas–liquid results, Chem. Eng. Sci. 138 (2015) 140–152.

[60] S. Vivekanand, V. Raju, Numerical study of the hydrodynamics and heat transfer characteristics of liquid–liquid Taylor flow in microchannel, Heat Transfer—Asian, Research 47 (6) (2018) 794–805.

[61] A. Abdollahi, R.N. Sharma, A. Vatani, Fluid flow and heat transfer of liquid-liquid two phase flow in microchannels: A review, Int. Commun. Heat Mass Transfer 84 (2017) 66–74.

[62] P. Sarkar, K. Singh, K. Shenoy, A. Sinha, H. Rao, S. Ghosh, Liquid–liquid two-phase flow patterns in a serpentine microchannel, Ind. Eng. Chem. Res. 51 (13) (2012) 5056–5066.

[63] C. Yao, H. Ma, Q. Zhao, Y. Liu, Y. Zhao, G. Chen, Mass transfer in liquid-liquid Taylor flow in a microchannel: Local concentration distribution, mass transfer regime and the effect of fluid viscosity, Chem. Eng. Sci. 223 (2020), 115734.

[64] A.-L. Dessimoz, L. Cavin, A. Renken, L. Kiwi-Minsker, Liquid–liquid two-phase flow patterns and mass transfer characteristics in rectangular glass microreactors, Chem. Eng. Sci. 63 (16) (2008) 4035–4044.

[65] A. Vansteene, J.-P. Jasmin, G.r. Cote, C. Mariet, Segmented Microflows as a Tool for Optimization of Mass Transfer in Liquid– Liquid Extraction: Application at the Extraction of Europium (III) by a Malonamide, Ind. Eng. Chem. Res. 57 (34) (2018) 11572–11582.

[66] H.H. Girault, Electrochemistry at liquid-liquid interfaces, Electroanal. Chem. 23 (2010) 1–104.

[67] B. Liu, M.V. Mirkin, Electrochemistry at microscopic liquid–liquid interfaces, Electroanalysis: An International Journal Devoted to Fundamental and Practical Aspects of, Electroanalysis 12 (18) (2000) 1433–1446.

[68] S. Liu, Q. Li, Y. Shao, Electrochemistry at micro-and nanoscopic liquid/liquid interfaces, Chem. Soc. Rev. 40 (5) (2011) 2236–2253.

[69] F. Kivlehan, Y.H. Lanyon, D.W. Arrigan, Electrochemical study of insulin at the polarized liquid– liquid interface, Langmuir 24 (17) (2008) 9876–9882.

[70] G. Laudadio, A.d.A. Bartolomeu, L.M. Verwijlen, Y. Cao, K.T. de, Oliveira, T. Noël, Sulfonyl fluoride synthesis through electrochemical oxidative coupling of thiols and potassium fluoride, J. Am. Chem. Soc. 141 (30) (2019) 11832–11836.

[71] Y. Cao, B. Adriaenssens, A.d.A. Bartolomeu, G. Laudadio, K.T. de, Oliveira, T. Noël, Accelerating sulfonyl fluoride synthesis through electrochemical oxidative coupling of thiols and potassium fluoride in flow, Journal of Flow Chemistry 10 (1) (2020) 191–197.

[72] G. Laudadio, W. De Smet, L. Struik, Y. Cao, T. Noël, Design and application of a modular and scalable electrochemical flow microreactor, Journal of flow chemistry 8 (3) (2018) 157–165.

[73] G. Laudadio, E. Barmpoutsis, C. Schotten, L. Struik, S. Govaerts, D.L. Browne, T. Noël, Sulfonamide synthesis through electrochemical oxidative coupling of amines and thiols, J. Am. Chem. Soc. 141 (14) (2019) 5664–5668.

[74] J. Dong, L. Krasnova, M. Finn, K.B. Sharpless, Sulfur (VI) fluoride exchange (SuFEx): another good reaction for click chemistry, Angew. Chem. Int. Ed. 53 (36) (2014) 9430–9448.

[75] T.A. Fattah, A. Saeed, F. Albericio, Recent advances towards sulfur (VI) fluoride exchange (SuFEx) click chemistry, J. Fluorine Chem. 213 (2018) 87–112.

[76] D. Ni, F.J. Hong, P. Cheng, G. Chen, Numerical study of liquid-gas and liquid-liquid Taylor flows using a two-phase flow model based on Arbitrary-Lagrangian–Eulerian (ALE) formulation, Int. Commun. Heat Mass Transfer 88 (2017) 37–47, https://doi.org/10.1016/j.icheatmasstransfer.2017.08.006.

[77] K. Yang, F. Hong, P. Cheng, A fully coupled numerical simulation of sessile droplet evaporation using Arbitrary Lagrangian-Eulerian formulation, Int. J. Heat Mass Transf. 70 (2014) 409–420, https://doi.org/10.1016/j.ijheatmasstransfer.2013.11.017.

[78] H. Jia, X. Xiao, Y. Kang, Investigation of a free rising bubble with mass transfer by an arbitrary Lagrangian-Eulerian method, Int. J. Heat Mass Transf. 137 (2019) 545–557, https://doi.org/10.1016/j.ijheatmasstransfer.2019.03.117.

[79] J. Donea, A. Huerta, J.-P. Ponthot, A. Rodríguez-Ferran, Arbitrary Lagrangian–Eulerian Methods, Encyclopedia of Computational Mechanics Second Edition, pp. 1-23. https://doi.org/https://doi.org/10.1002/9781119176817.ecm2009.

[80] M.P. Andersson, M.V. Bennetzen, A. Klamt, S.L.S. Stipp, First-Principles Prediction of Liquid/Liquid Interfacial Tension, J. Chem. Theory Comput. 10 (8) (2014) 3401–3408, https://doi.org/10.1021/ct500266z.

[81] F.P. Bretherton, The motion of long bubbles in tubes, J. Fluid Mech. 10 (2) (1961) 166–188.

[82] P. Aussillous, D. Quéré, Quick deposition of a fluid on the wall of a tube, Phys. Fluids 12 (10) (2000) 2367–2371, https://doi.org/10.1063/1.1289396.

[83] Y. Han, N. Shikazono, N. Kasagi, Measurement of liquid film thickness in a micro parallel channel with interferometer and laser focus displacement meter, Int. J. Multiph. Flow 37 (1) (2011) 36–45, https://doi.org/10.1016/j.ijmultiphaseflow.2010.08.010.

[84] M. Eain, V. Egan, J. Punch, Film thickness measurements in liquid–liquid slug flow regimes, Int. J. Heat Fluid Flow 44 (2013) 515–523, https://doi.org/10.1016/j.ijheatfluidflow.2013.08.009.

[85] D.A. Hoang, V. van Steijn, L.M. Portela, M.T. Kreutzer, C.R. Kleijn, Benchmark numerical simulations of segmented two-phase flows in microchannels using the Volume of Fluid method, Comput. Fluids 86 (2013) 28–36, https://doi.org/10.1016/j.compfluid.2013.06.024.

[86] J. Ratulowski, H.C. Chang, Marangoni effects of trace impurities on the motion of long gas bubbles in capillaries, J. Fluid Mech. 210 (1990) 303–328, https://doi.org/10.1017/S0022112090001306.

[87] D.R. Langewisch, J. Buongiorno, Prediction of film thickness, bubble velocity, and pressure drop for capillary slug flow using a CFD-generated database, Int. J. Heat Fluid Flow 54 (2015) 250–257, https://doi.org/10.1016/j.ijheatfluidflow.2015.06.005.

[88] Z. Peng, L. Ge, R. Moreno-Atanasio, G. Evans, E. Doroodchi, VOF-DEM study of solid distribution characteristics in slurry Taylor flow-based multiphase microreactors, Chem. Eng. J. 396 (2020), 124738, https://doi.org/10.1016/j.cej.2020.124738.

[89] L. Ge, Z. Peng, R. Moreno-Atanasio, E. Doroodchi, G.M. Evans, Three-Dimensional VOF-DEM Model for Simulating Particle Dynamics in the Liquid Slugs of a Vertical Gas–Liquid–Solid Taylor Flow Microreactor, Ind. Eng. Chem. Res. 59 (16) (2020) 7965–7981, https://doi.org/10.1021/acs.iecr.0c00108.

[90] B. Ahmed-Omer, J.C. Brandt, T. Wirth, Advanced organic synthesis using microreactor technology, Org. Biomol. Chem. 5 (5) (2007) 733–740, https://doi.org/10.1039/B615072A.

[91] M.J. Martinez, K.S. Udell, Axisymmetric creeping motion of drops through circular tubes, J. Fluid Mech. 210 (1990) 565–591, https://doi.org/10.1017/S0022112090001409.

[92] E. Lac, J.D. Sherwood, Motion of a drop along the centreline of a capillary in a pressure-driven flow, J. Fluid Mech. 640 (2009) 27–54, https://doi.org/10.1017/S0022112009991212.